



**Politecnico
di Torino**

Master of science in Mechanical Engineering

Master's degree Thesis

Thermal Simulation of Selective Laser Melting Process

Candidate:

Nasir Zamindar

Student ID: 224454

Supervisors:

Prof. Cristiana Delprete, Supervisor

Dr. Abbas Razavykia, Co-supervisor

Politecnico di Torino

October 2021

Acknowledgment

I would like to express my deepest appreciation to my supervisor, Professor Cristiana Delprete, for her contributions. I would like also to express my sincere gratitude to my co-supervisor, Dr. Abbas Razavykia, for all his wise advice, helping attitude and kindness.

Finally, I am grateful with my family for their support.

Abstract

Through thermal simulation of Selective Laser melting (SLM), one can predict the thermal distribution over the power bed during the process without performing practical experiments. In this case, the production of a piece can be improved and the possible failure in the final part would be prevented. In SLM there is high temperature gradient which leads to imposing thermal stress due to deformation and, finally, fracture of workpiece. The duration of simulation depends on several factors such as thermal properties (specific heat and thermal conductivity) of the material (constant or temperature dependent), scan area, meshing, number of laser scan tracks, and laser scan velocity value. The simulation is done by adopting Gaussian profile to resemble the laser movement. Gaussian beam is normally used in optics, and it mathematically consists of laser power intensity. During simulation, parameters such as laser power intensity, laser radius, hatch space, scan strategies, laser scanning speed and environment temperature are investigated.

The software used for simulation is Ansys version 18.2 in the workbench system which solves the heat transfer equation by finite element analysis in order to obtain the temperature distribution on the powder bed. The investigated material is Ti-6Al-4V powder.

Results as indicated in the literature indicate that by increase of laser power and decrease of scanning speed separately, the temperature obtained on the powder bed increases, but the order and amount of increase reached by power rise is much higher. In addition, with increasing laser power intensity, the melt pool dimensions, i.e., length and depth increase significantly.

Two strategies, namely, parallel and zigzag, have been adopted to direct the path of the laser. As results indicate, for the low amount of power there is no significant difference in the maximum temperature for both strategies obtained on the power bed while for increased power the zigzag structure represents higher temperature. In general, the second and third scan paths indicate higher temperature compared to the first track since the heat produced by the laser is accumulated. As a matter of fact to understand the effect of strategies, the scan domain should be changed.

Contents

Abstract.....	iii
List of Figures.....	vi
List of Tables	ix
Nomenclature.....	x
1 Introduction to Additive Manufacturing.....	1
1.1 History.....	1
1.2 AM Processes.....	2
1.2.1 Sheet Lamination.....	3
1.2.2 Direct Energy Deposition.....	4
1.2.3 Binder Jetting	5
1.2.4 Selective Laser Melting	6
1.3 Cost of Process.....	8
1.4 Application	9
1.4.1 Automative Industry.....	9
1.4.2 Aeronautical Industry	9
1.4.3 Medical Industry.....	10
1.4.4 Microscale Application.....	10
1.5 Materials.....	11
1.5.1 Titanium	12
1.5.2 Titanium Alloy (Ti6-Al-4V).....	13
1.5.3 Powder Absorptivity	14
1.6 Metallurgical Defects.....	14
1.6.1 Balling.....	14
1.6.2 Crack.....	16

1.6.3	Post-process Heat Treatment	16
1.6.4	Powder bed Pre-heating	17
1.6.5	Powder Layer Thickness.....	18
1.7	Scan Strategy.....	19
1.7.1	Hatch Space.....	20
1.8	Melt Pool	22
1.8.1	Laser beam Size.....	22
2	Model Description	24
2.1	Heat Transfer Equations	24
2.1.1	Initial & Boundary Conditions	26
2.2	Laser Heat Source	27
2.2.1	Numerical Model.....	28
2.3	Experimental Methodology.....	34
3	Results	38
3.1	Scan Strategy.....	38
3.2	Power effect.....	43
3.3	Scanning Velocity effect	45
3.4	Residual stress.....	47
	References	49
	Appendix	54

List of figures

1.1	Schematic of Sheet Lamination process [8].....	3
1.2	Schematic of DED process for (A) laser beam and (B) electron beam sources [10].	4
1.3	Binder jetting process schematic [5].....	5
1.4	Characteristics of SLM process [13]	6
1.5	SLM technology configuration [16]	7
1.6	Parts produced by SLM [19].....	10
1.7	SLM process preferences in medical devices compared to other technologies[22]	11
1.8	Phase diagram of titanium alloys depending on elements in alloys. [24] ..	12
1.9	Schematic balling phenomenon in SLM[19].....	15
1.10	Crack representation in SLM process due to thermal stress[19].....	16
1.11	Layer thickness [17].....	18
1.12	Various patterns of island scanning strategy [30].....	20
1.13	The pattern of hatch space indicating the overlap of two subsequent lasers[34]	21
1.14	Melt pool configuration of high density laser for (a) small laser beam diameter and (b) large laser beam diameter[36].....	23
2.1	Schematic of heat transfer formations during Selective Laser Melting	25
2.2	Flowchart of SLM process simulation with ANSYS.	29
2.3	Three-dimensional finite element model of workpiece during SLM.	30
2.4	Scan strategies in SLM process: (a) parallel - (b) zigzag	31
2.5	Introduction of gaussian laser function to get APDL commands.	32

2.6	Convection boundary has been defined with yellow color and radiation as blue color.....	33
2.7	Schematic of experimental Setup	34
2.8	Experimental thermal distribution by Kolossov et al at X= 1.85, Z= 2.0...	35
2.9	Mesh developed for simulating experimental work done by S. Kolossov et al [10].....	36
2.10	Comparison of simulated result obtained for experimental work done by S. Kolossov et al [10].....	36
2.11	Scan strategies in SLM process: (a) parallel - (b) zigzag Fig. 2.10 The temperature at the end of 1st scan track is around 2000°C.....	37
3.1	Temperature distribution of first, second and third laser scan tracks adopting parallel strategy at velocity of 10mm/s for p=2W	38
3.2	Temperature distribution of first, second and third laser scan tracks adopting zigzag strategy at velocity of 1mm/s for p=2W	39
3.3	Temperature distribution of first, second and third laser scan tracks adopting parallel strategy at velocity of 10mm/s for p=10W	40
3.4	Temperature distribution of first, second and third laser scan tracks adopting zigzag strategy at velocity of 10mm/s for p=10W	40
3.5	Thermal profile of P=10w at 10mm/s when 0.073 second has passed during SLM process.	41
3.6	Thermal profile of P=10w at 10mm/s when 0.257 second has passed during	
3.7	Thermal profile of P=10w at 10mm/s when 0.0643 second has passed during SLM process.....	41
3.8	Thermal profile of P=10w at 10mm/s when 0.179 second has passed during SLM process.	42
3.9	Thermal profile of P=10w at 10mm/s when 0.253 second has passed during SLM process.	42
3.10	Temperature distribution of first, second and third laser scan tracks adopting parallel strategy at velocity of 1mm/s for p=2W	42
3.11	Temperature distribution of first, second and third laser scan tracks adopting parallel strategy at velocity of 1mm/s for p=10W	43

3.12	Maximum temperature distribution across the third laser track for power of 2 and 10 watt.	43
3.13	Temperature gradient of laser heat source along scan direction from center of laser	44
3.14	Temperature profile of power at 10 watt for two scan velocity of 1 and 10mm/s across time.....	44
3.15	Melt pool dimensions including length and depth at power level of 10W for (a) : 1mm/s and (b) : 10mm/s.	45
3.16	Schematic of coupling of thermal and structural system	46
3.17	Equivalent Von mises stress profile for (a) : $p=2w$ and scan velocity of 10mm/s , (b) : : $p=10w$ and scan velocity of 10mm/s.	48

List of Tables

1	Thermal properties of bulk Ti6-4Al-6V [9]	9
2	Physical properties of bulk Ti6-4Al-6V [9]	9
3	Parameters related to numerical finite element model during SLM process.	10
4	Laser characteristics by Kolossov et al[10]	12

Nomenclature

ρ	density, kg/m ³
c_p	specific heat capacity, J/(kg.K)
k	thermal conductivity, W/(m.K)
t	time, s
Q	heat generation per volume, W/m ³
h	coefficient of heat convection, W/(m ² .K)
T	temperature of powder system, °K
T_0	ambient temperature, °K
q_{conv}	heat convection, W/m ²
q_{rad}	heat radiation, W/m ²
ε	emissivity
σ	Stefan–Boltzmann constant
Q_s	input heat source flux, W/m ²
A	laser energy absorptivity of a material
P	laser power, W
R	effective laser beam radius, m
r	radial distance from a point to the center of laser beam, m
n	normal vector
x, y, z	spatial coordinates, m

Chapter 1

Introduction to Additive Manufacturing

Three-dimensional (3-D) printing, which is also known as additive manufacturing or rapid manufacturing, is considered a modern advanced manufacturing technology with numerous applications in industry. Three-dimensional printing takes advantage of various basics such as computer, numerical control, machinery, material, etc. [1]. During the processes of additive manufacturing the quality of built part could be influenced depending on several reasons such as parameters of process and material where these parameters could be experimented through numerical simulation [2]. In this case the thermal simulation could play an important role to adjust the parameters in order to avoid the appearance of defects [3].

1.1 History

Looking at its history briefly, three-dimensional production layer by layer came into mind before the appearance of additive manufacturing. It can be expressed that in the year 1902 Peacock ignited the first spark by creating horseshoes in the form of laminate. Around fifty years later in 1952 the advantages of the manufacturing layer by layer were described by Kojima. The period of the 60-80s was a key moment since several patents occurred which could contribute to form the concept of layer by layer 3-D production and, consequently, build prototypes with various processes. Stereolithography apparatus-1(SLA-1) appeared as the first rapid

prototyping mechanism for sale in 1987 in this process, the UV laser causes photopolymerization as the laser scans the resin, the solid layer is formed. One year later, in 1988, Ciba-Geigy first acrylate resins were presented into the industry. At the same time, Solid Object Ultraviolet Plotter (SOUP) which was similar to stereolithography process sent to the market by Mitsubishi's CMET in Japan. Meanwhile, resins of epoxy which were used as material for photopolymerization process. The form of additive manufacturing that we deal with today is a result of the great revolution that took place in the years 1991 and 1993. The new systems such as Solid Ground Curing, Fused Deposition Model, Laminated Object Manufacturing, Selective Laser Sintering and direct shell production casting reached the market at the same time. In the current market of Additive Manufacturing, FDM plays an important role while LOM is not used widely, and SGC was not at all successful in the market. In this period the shares of SLS and DSPC in additive manufacturing cannot be neglected where DSPC has changed compared to its first technology. New technologies related to additive manufacturing such as Selective Laser Melting of metals, Laser Engineered Net Shaping, Ultrasonic Additive Manufacturing, Aerosol Jet Printing have taken shape fast in the last twenty years. Along with these processes and considering different applications, materials such as metals, polymers, ceramics, composites have been in the track of advance. Nowadays, additive manufacturing is standing far away from its initial purpose to be just a prototype. In other words, it is used to build end products of tiny dimensions to very large ones, for instance, passenger cars could be made with this technology [4].

1.2 AM Processes

Additive manufacturing is based on layer-by-layer technique which enables construction of parts of difficult geometries, and it would be considered a revolution in the current manufacturing industry [1]. Additive manufacturing process starts with a software model (CAD) which describes the three-dimensional geometry, then the file is converted into STL format which is the basis for numerical calculations of slices. Afterwards, the file is input to Additive Manufacturing machine and before the building process begins, the machine must be set up [5]. There are various processes used in additive manufacturing among them Material Extrusion, Binder Jetting, Directed Energy Deposition, Sheet Lamination and Selective Laser Melting are most important [4].

1.2.1 Sheet Lamination

Sheet Lamination process is also called Laminated Object Manufacturing, where in this process ultrasonic is used as a source of energy and sheet of metal is employed as a feeding material. In the Sheet Lamination, melting is not the factor for binding the sheets, but instead, the diffusion and pressure contribute to the formation of the final object. By performing polishing, proper surface quality is obtained [7].

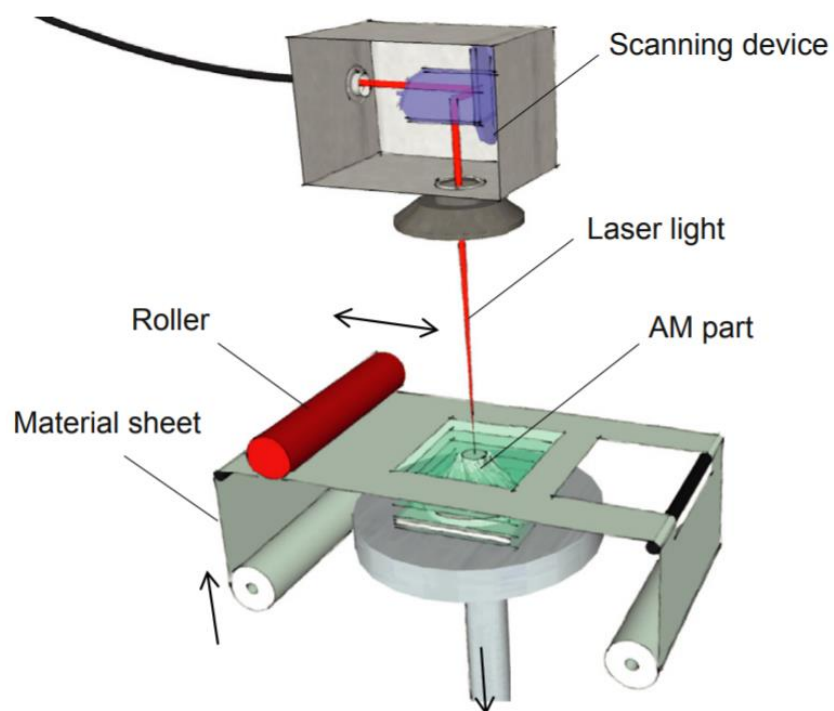


Fig. 1.1 Schematic of Sheet Lamination process [8].

1.2.2 Direct Energy Deposition

In Directed Energy Deposition (DED), the heat is introduced by laser or plasma to melt the powder particles where materials of filler in the form of wire or powder are included. In this process, the deposition is done by movement of the nozzle. Then, according to the CAD design data, the parts would be built layer by layer. The DED process is mainly used for improving the quality of existing objects, however, it can be used to build final parts if coupled with CNC machining. The weaknesses of DED process can be mentioned as requiring a great amount of inert gas and low surface quality which needs performing post processing [9].

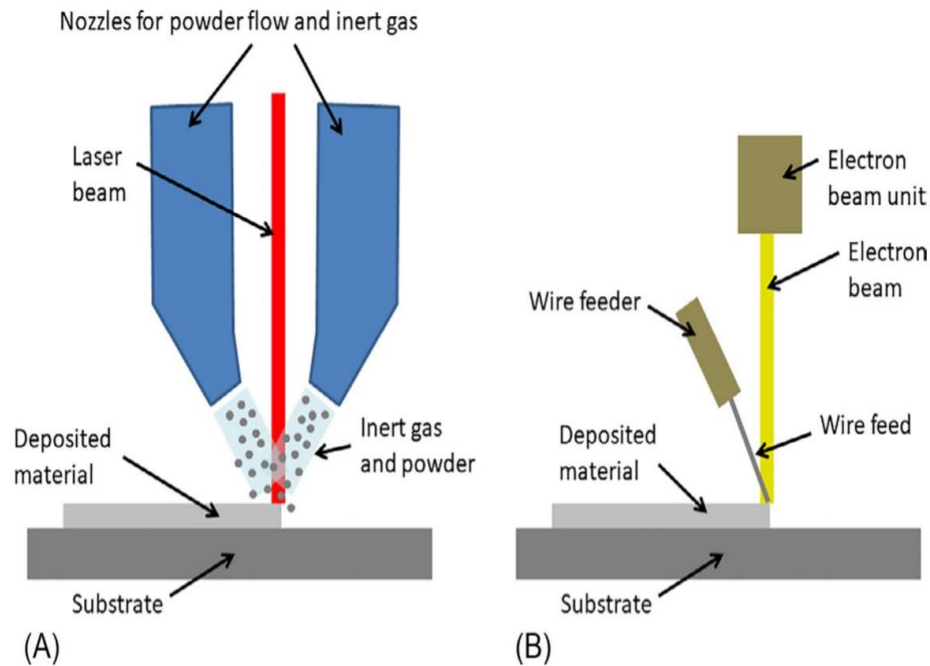


Fig. 1.2 Schematic of DED process for (A) laser beam and (B) electron beam sources [10].

1.2.3 Binder Jetting

In Binder Jetting (BJ), which is also called inkjet three-dimensional printing, the liquid agent is injected on the powder layer to adhere the powder particles by adopting one or more nozzles. According to the design, the movement of the nozzle continues to reach the initial layer of powder. The final part is created by building all the layers. Post processing is done on the final adhesive part known as the green body.

When the bonding element is taken out, it may cause shrinkage of part for metallic parts. Therefore, special heat treatment such as sintering and burning of bonding agent would be required to gain proper mechanical properties [11].

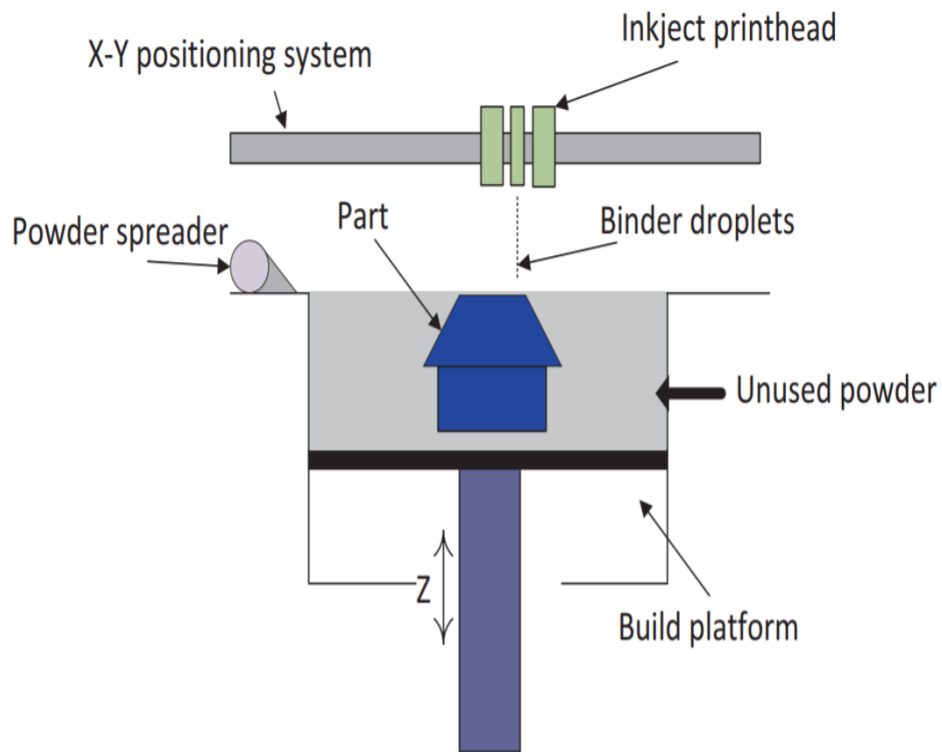


Fig. 1.3 Binder jetting process schematic [5].

1.2.4 Selective Laser Melting

During the Selective Laser Melting process which is also called laser powder bed fusion (LPBF), high thermal energy originating from one or more lasers selectively fuses and melts the powder bed, then it gets solidified by proper cooling, then the platform moves down to have deposition of next layer. Finally, the workpiece would be built layer by layer. Through patterns made in a computer the laser can move in a certain direction; consequently, the melting process is done selectively, and the desired three-dimensional part is obtained. Metal powder made of titanium, aluminum, stainless steel, copper, and superalloys are widely used in the Selective Laser Melting process. One of the problems of SLM process is losing recyclability of powder materials when they are oxidized during the melting process, therefore some amount of powder is lost. Another weakness would be attributed to the inability to build overhanging shapes as the conduction of heat is less below the cooled down layer. The range of powder size used in most of the SLM process is between $20\mu\text{m}$ to $50\mu\text{m}$ [10]. The evaluation of the final product made by SLM process would be done by properties such as surface quality, mechanical properties and etc. which have been shown in Fig 1.4 [13].

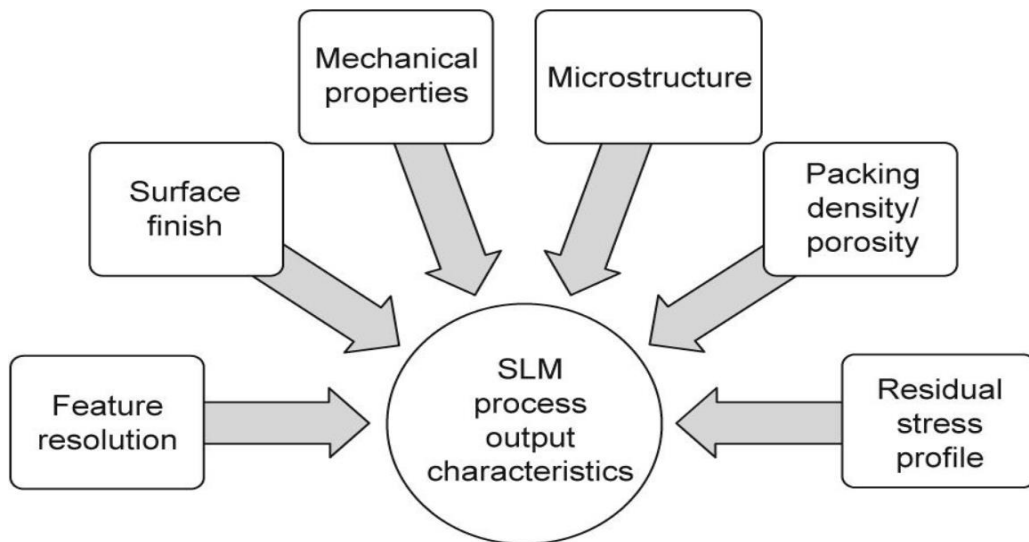


Fig. 1.4 Characteristics of SLM process [13].

Lack of appropriate melting and cooling which are influenced by scanning characteristics would lead to defects on final built 3-D geometry such as balling and distortion. Consequently, it is very important to attain a well-constructed molten pool. Since in high thermal distribution there is high level of reactivity [14]. Adopting SLM process has some advantages such as the possibility of employing different materials to build up the object, economical cost, ability to create complex geometries and being able to adjust the properties. However, there are some disadvantages like applying power with high intensity, restrictions in the speed of process and time-taking optimization of the SLM parameters [15]. The process of SLM has been shown in Fig.1.5.

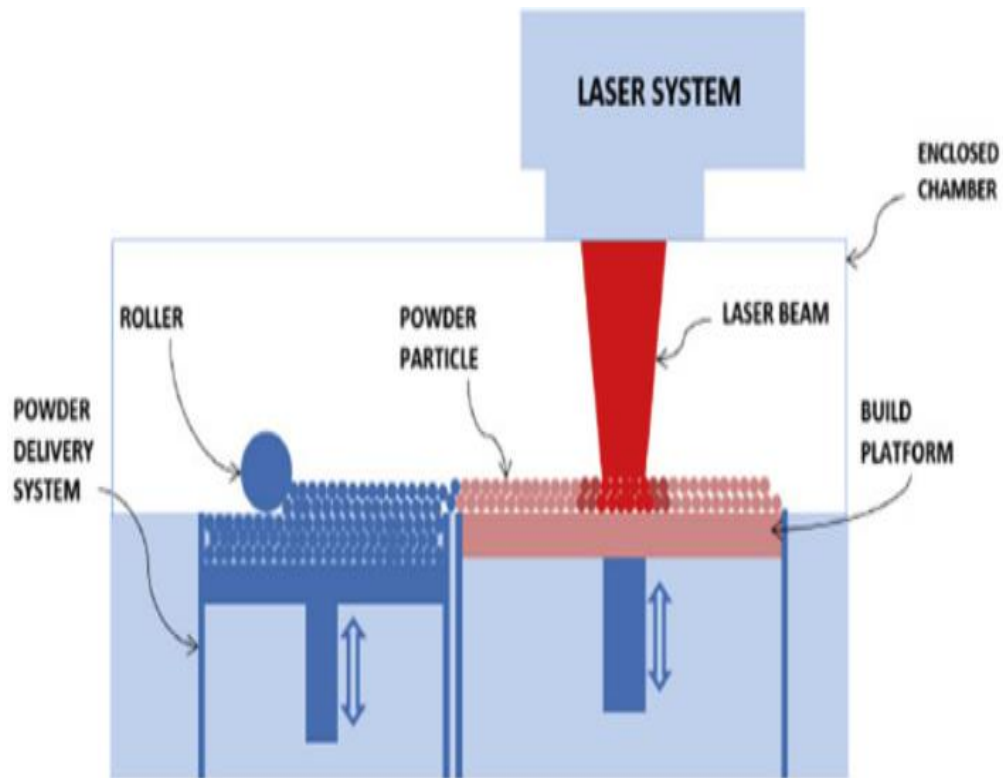


Fig. 1.5 SLM technology configuration [16].

1.3 Cost of Process

During the SLM process, the primary factors that determine the cost of the process are the powder which is used for melting and time taken for the production of part depending on the machine. As a result, the built part can be expensive accordingly. Since patents have limited time for existence, after a period the production technologies related to the SLM process would increase and the cost related to manufacturing would decrease. If comparing the price between bulk and powder of the same material, powder costs more particularly for the process of SLM where special processing is done on powder to obtain a specific size of powder or shape and the powder is patented, which adds extra cost to that.

However, for the powders made of metal, the cost can be decreased if no processing is done or in the case that the rate of production of a specific powder is high, then the price is expected to be cheap. In the SLM process the degree of complexity of part geometry does not influence the time of the process and no extra cost is included. The SLM process is more economical for short production as the costs are balanced. If compare the SLM process with the machining process and consider the titanium powder which is considered expensive by doing machining, the cost would be high as powder is wasted, and it can be saved in the case of the SLM process. Mass producing parts with simple geometry through SLM process is not economical, but if products are complex in geometry, and the amount of production is limited, then it can be considered economical [17]. In general, the cost associated with the SLM process involves design, production and post-processing. There are also costs related to the utility, inert gas etc. However, in the case of mass production with the same geometry, the cost of design is not considered. The costs of production are relevant to materials, machine setup and time of running. The powder of Ti6Al4V would cost approximately €200 to €400 per kilogram. The weight and amount of discarded metal powders determine the cost. The post-processing costs depend on heat treatment, finishing of surface and etc. [18].

1.4 Application

According to the observation, the texture of products built by Selective Laser Melting has good quality and microstructure is well-built enough compared to other techniques of additive manufacturing. Some other processes may require higher temperature and more pressure, which means more cost and energy, however, in SLM the cost is reduced. The SLM has quite high accuracy of about 0.1 millimeter, which is useful in applications where accuracy is of great importance in order to build parts containing complex geometries, namely in vehicle, aerospace, medical pieces and etc. As an example, building pipes of complex structures located in rows of blades of spacecraft is not possible using traditional manufacturing methods, however, it can be done successfully adopting SLM [19].

1.4.1 Automotive Industry

In the automotive sector, SLM process would be so influential since it provides proper flexibility in design and material selection. For example, electric motor used in electric, or hybrid vehicles can be produced in a creative way adopting soft magnetic alloy which enables improving the thermal properties of electric motor [20].

1.4.2 Aeronautical Industry

By adopting SLM process in the new generation of aircraft, the parts such as the engine would have less weight and, consequently, the usage of fuel and production of CO₂ would be decreased. Obviously, by producing aeronautical parts, the efficiency would increase since the weight and gas production of aircraft diminish. Therefore, the SLM process can play an important role for producing aeronautical components [21].

1.4.3 Medical Industry

Regarding the application of SLM in the medical industry, implants made of metals are used to replace body organs in case of cosmetic or curing. The cost of metallic implants would be high to produce since they should be compatible with living organs and be shaped as medical stuff. Advantages of adopting SLM process in medical devices compared to other manufacturing technologies have been shown in Fig. 1.7 [22].

1.4.4 Microscale Application

In addition to the mentioned applications, the SLM process can be applied to produce microscale components such as micro-mechanical parts and micro-motors. By employing SLM process in microscale, one can take advantage of the reduced time for production and simple processing. In micro SLM process, powder particle sizes of the range $20\ \mu\text{m}$ to $50\ \mu\text{m}$ and layer with thickness of $20\ \mu\text{m}$ to $100\ \mu\text{m}$ are adopted. [13]

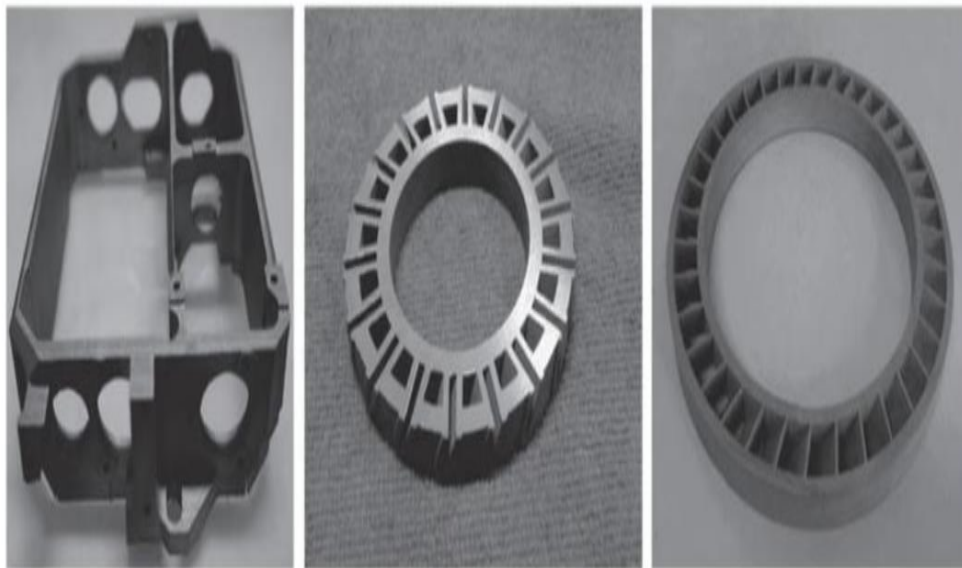


Fig. 1.6 Parts produced by SLM [19].



Fig.1.7 SLM process preferences in medical devices compared to other technologies [22].

1.5 Materials

Titanium, iron, and nickel are among the most common metals used in SLM process which are chosen depending on the application, however other metals such as aluminum, copper and tungsten have been experimented in research. The ferrous metals would offer proper flexibility during the SLM process so that the built parts have good porosity, which could be a great advantage since the weight of high-density steel can be reduced. The most common used ferrous metal is 316L stainless steel. Nickel-based alloys play role in experiments among them Inconel is the most common. Nickel based alloys are used in case of high thermal distribution and can attain a stable melt pool [23].

1.5.1 Titanium

The element of Titanium is found on the crust of Earth in a great amount; however, reaching pure dense Titanium is impossible. Therefore, it should be further processed, and extra cost would be added. Titanium alloys are mostly preferred to other metals due to their high strength as they are light also because of their resistance to corrosion. The tiny disadvantage of Titanium alloys would be their oxidization at high temperature. Titanium alloys with the base of aluminum indicate applications at higher temperature compared to other traditional titanium alloys. Crystallization of titanium and its alloys at low temperature is in the form of hexagonal close packed (HCP) and when crystallization occurs at high temperature it is in the form of body-centered cubic (BCC). These two structures are called α and β phases respectively. Regarding the plastic deformation of the two structures, HCP titanium has lower value compared to BCC titanium. Regarding the diffusion phenomenon, BCC titanium has higher value compared to HCP titanium since in HCP package of atoms are denser.

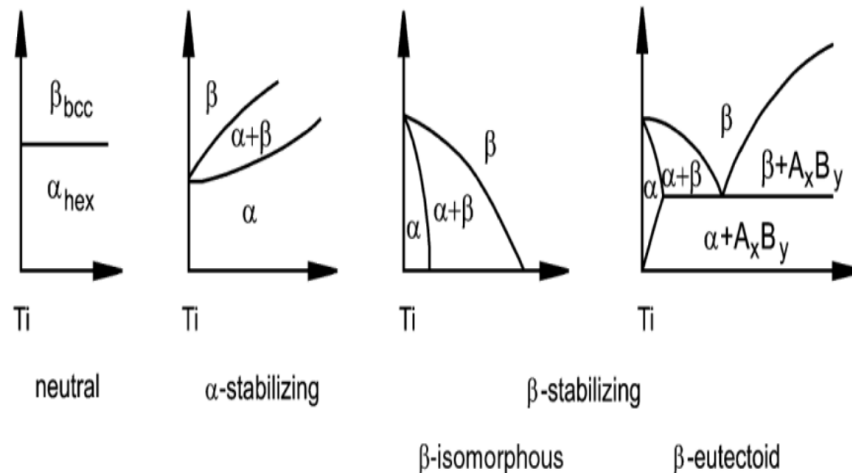


Fig. 1.8 Phase diagram of titanium alloys depending on elements in alloys [24].

The amount of diffusion and plastic deformation depending on the microstructures would define the mechanical property of titanium alloys. Transformation temperature is the basis for classification of titanium alloys as beta stabilizer, alpha stabilizer and neutral. In titanium alloys containing the beta stabilizer, the temperature corresponding to the beta phase decreases while alloys containing alpha stabilizer, the temperature relating to the alpha phase is increased whereas neutral type has no significant impact on temperature. Aluminum is most used as an alpha stabilizer in titanium alloys and among elements of beta stabilizer molybdenum and vanadium are the most used. Depending on the alpha and beta phases, the titanium alloys are divided. For example, the pure titanium and alloys containing alpha stabilizers place in the alpha alloys category. The sum of both alpha and beta phase which is also known as martensite is the most common category of titanium alloys. Microstructure and composition of chemicals are the key factors that influence the mechanical properties of titanium alloys where the fraction of alpha and beta phases determine the chemical composition. Nowadays, numerous titanium alloys are discovered where about twenty of them are commercialized [24].

1.5.2 Titanium Alloy (Ti-6Al-4V)

Among $\alpha + \beta$ alloys, Ti-6Al-4V is one the most adopted with good mechanical properties and large domain of temperature with numerous applications in industry. The Ti-6Al-4V alloy can be strengthen by adding alpha and beta stabilizers. The mechanical property of titanium alloys can be increased by processing, alloying, and creating composite materials [24]. Characteristics of composite materials such as MMCs which are metal matrix composites are obtained by the combination of metal and ceramic properties with proper conduction and stiffness, MMCs however are not economical. When using the MMCs during the SLM process, fusing and chemical reaction occur at the same time where the laser moves. At the end of process, complex composite object with desired properties is obtained [25].

1.5.3 Powder Absorptivity

The powder is an important element when dealing with the SLM process as it melts and then solidifies when the laser makes contact with it. The amount of molten area is proportional to the rate of absorption. There is a direct relation between the powder absorption rate where metallic powder absorptivity increases as the laser wavelength decreases. The absorptivity of powders such as Ag and Cu is very low at high laser wavelength, and they are not used in the SLM process. In this regard, alloys with a base of titanium and iron are among the most used in the SLM process. During the SLM process, the laser strikes the metal powder, part of energy is absorbed by the powder, part of energy reflected and the remaining energy transfers through powder, however, the transmission energy would be considered zero for metal powders. In SLM, when the reflection of energy by the metal powder is high the absorption rate of powder decreases. Consequently, the molten area is not formed. In the SLM process, usually a laser emitter with a wavelength of 1064-nm is used, however because the reflectivity of light in this wavelength is low, limited energy is absorbed by the metal powder. Increasing laser beam power is not an appropriate solution to improve absorption since the thermal gradient and the level of residual stress increase. The level of absorption and reflection of the laser beam during the SLM process would determine the efficiency of melting. In SLM process, to increase the absorption, a short wavelength is adopted. Among the laser sources, semiconductor diode lasers have the highest efficiency as they introduce a wide range of wavelengths (405–3300nm). In addition, Diode lasers have less operation cost compared to fiber lasers [26].

1.6 Metallurgical Defects

1.6.1 Balling

Beside the frequent use of SLM technology to build complex parts, there are some disadvantages which lead to deterioration of surface quality. During the SLM process, after building the first layer, the metal powder grains should be inserted orderly to make the next layer, but sometimes the grains have distance from each other. This problem or better to say defect which is called balling can prevent from creating part with good quality when SLM is in progress. It is called balling since the group of spherical particles appear on the surface of metal and in this way do

not allow the formation of melting in a uniform way. Consequently, when balling appears, the roughness of the metal surface intensifies, and the quality deteriorates. The pores appear inside the metal because of the balling defect. In addition, strong friction would be observed between the powder roller and the previous layer built due to the balling defect. The later would be considered as high failure since the velocity of the roller would decrease or even stop, which would prevent from processing the part. Balling defect can be seen from the wettability aspect between the melted flow and the bulk face. If consider the angle between interface tensions of liquid-solid and liquid-gas faces, for angles higher than 90° the balling defect dominates while for angles less than 90° there would be no balling and a melt pool would appear on top of the first layer without making pores. Another problem that one might encounter in SLM process is porosity, which is the consequence of the balling defect, where pores appear on metal surface due to space between metal grains and decrease the quality.

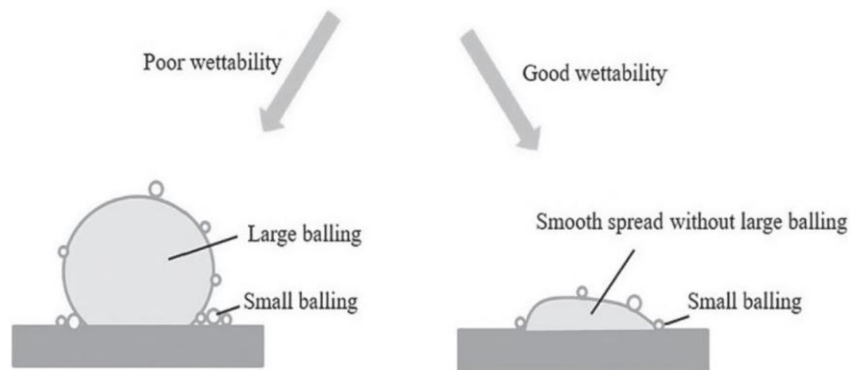


Fig. 1.9 Schematic balling phenomenon in SLM [19].

During building the second layer, the spaces between metal grains lead to the formation of porosity in the final part. During the SLM process, a fraction of inert gas which is available for protection solidifies and consequently the number of pores increase in the melt pool [19].

1.6.2 Crack

Another reason for the formation of pores in the SLM process could be the existence of cracks. Cracks form mainly due to high temperature difference between the two phases of melting and cooling where the part experiences local deformation in the melt pool where there is high temperature and after that, it cools down. The compressive and tension stress dominate the melt pool domain, and the overall stress exceeding the yield stress of material is the origin of crack. The existence of crack causes deterioration of part quality. Hot isostatic method is adopted to decrease the cracks formed inside the part [19].

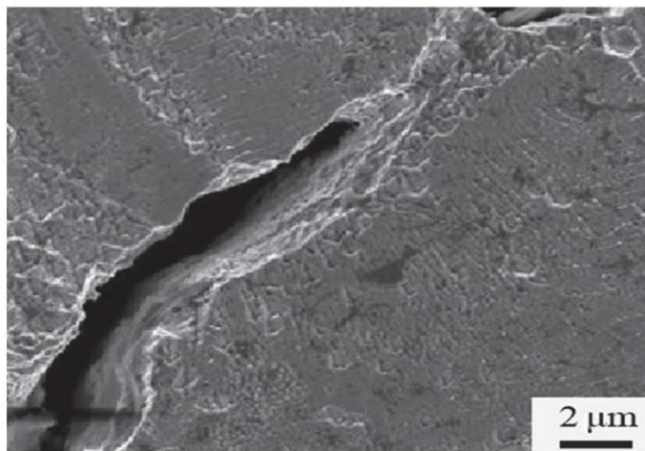


Fig. 1 .10 Crack representation in SLM process due to thermal stress [19].

1.6.3 Post process heat treatment

Internal stresses are of importance during the SLM process of Ti6Al4V since they cause the appearance of defects in the final part. In order to solve this problem, heat treatment can play an important role to improve the microstructure of the final piece which is exposed to high power density of the laser and other process parameters which intensify the thermal gradient formed on the part. To minimize the strain, the

heat treatment process is performed when the part has not been segregated from the substrate. The first step in heat treatment is increasing the temperature to, for example, 900°C which is less than the melt temperature of Ti6Al4V, then cooling the Ti6Al4V workpiece to a temperature, for instance, 500°C without outer influence and finally, rapid cooling to the ambience temperature. The ductility of Ti6Al4V is low while by adopting the heat treatment process its ductility increases. The heating treatment depends on the beta-transus temperature. The values of the phases alpha and beta change if the heating is higher or lower than the beta-transus temperature. The rate of cooling phase during the heat treatment influences the morphology. The increased heating temperature in the heat treatment process would increase the fatigue strength and decrease the possibility of crack initiation. The specimens heat treated at lower temperature represent higher tensile stress and finer grains, so better mechanical properties [27].

1.6.4 Powder bed pre-heating

The high thermal distribution formed on the powder bed by high laser intensity during the SLM process would create a high amount of residual stress on the workpiece. The rapid cooling and heating done during the SLM process of Ti6Al4V powder would decrease the ductility and increase the residual stress of the final built part which can lead to failure such as cracks. Therefore, by adopting pre-heating with high temperature during the feedstock of Ti6Al4V, the ductility would increase, and the mechanical properties increase as cooling is done in a controlled way. Comparing the heat treatment with powder base preheating can mention that the heat treatment process is more expensive and time-consuming to have an impact on the mechanical properties. During the pre-heating process in the SLM, the maximum temperature that has been applied is around 400°C, however, in the most commercialized machine due to design of systems and functionality the preheating temperature is around 200°C. The titanium alloy Ti6Al4V is the sum of alpha and beta if during the SLM process the rate of cooling increases the microstructure of alloy turns into martensite which has lower ductility so application of preheating can improve the ductility of martensite microstructure, however the proper temperature to reach less internal stress and high mechanical property has not found knowing that the temperature range required to decompose the martensite is between 600 and 650°C. During the preheating process of the powder bed, it can be observed that by increasing the preheating temperature, the rate of cooling

decreases, which leads to decrease of thermal gradient and residual stress and increase of yield strength [28].

1.6.5 Powder Layer Thickness

Powder layer thickness which is the thickness of powder bulk placed at the bed is the same as thickness of slice defined by 3D CAD model. The powder layer thickness influences the time required to build up the part. The time to produce the part decreases when the thickness of the powder layer increases while the reduction of powder layer thickness would lead to proper precision. Laser beams of high energy intensity would be required in the case that the layer of powder thickness increases, however laser beams with high power can lead to distortion on the part. With decreasing the thickness of the powder layer, the laser beam of lower energy intensity would be required, however the cost of production would increase. There is direct dependence of the level of strength and plastic deformation on the thickness of powder layer. By increasing the thickness of the powder layer, the level of plastic deformation increases, which means lower strength. Furthermore, the vertical workpieces indicated higher plastic deformation and so less strength while horizontal workpieces showed better mechanical properties [29]. During the SLM process, using the low-thickness powder helps to obtain good surface quality as roughness decreases. The decision to insert powder layer with high or low thickness is related to the structure of part that is going to be built where for multiple shape part, edges in vertical direction of part the layer thickness is increased and for inclined edges the layer thickness should be decreased in this way the time to produce the part is optimized and surface quality is protected [17].

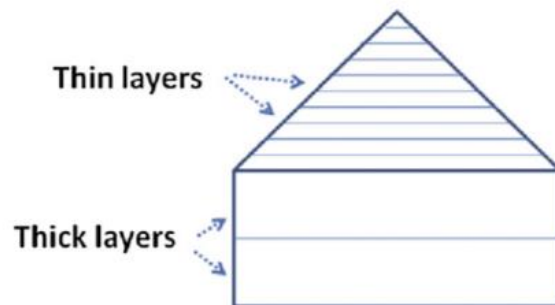


Fig. 1.11 Layer thickness selection [17].

1.7 Scan Strategy

Depending on the type of laser scan strategies, i.e., parallel, or zigzag, different thermal gradient and therefor various residual stresses and mechanical properties are obtained during the SLM, consequently, the final microstructure is achieved. The high level of residual stress would create a workpiece with distortion in a non-uniform way. Apparently, to get proper properties, the scan strategy should be optimized to control the level of residual stresses. Strategy of scanning can be defined according to the order of scanning, path of lasers, hatch space and rotation angle of vector. Among the available scanning strategies, bidirectional (zigzag) and unidirectional laser paths are more used where they both have the same vector length but different direction. In the unidirectional strategy, the laser follows the same direction while for the bidirectional strategy the laser follows reverse paths. It should be considered that by increasing the length of scanning, more residual stresses would appear on the final part due to accumulation. Instead of scanning paths with big length, island scanning strategy would be adopted to build large objects with proper quality where in this strategy the total area of scanning consists of smaller scanning cells. In the figure given below, various island scanning patterns have been adopted which have different cooling rates and time to solidify. When the laser is moving along its path, a high amount of residual stress is formed on the path since the thermal gradient increases along the path, however it decreases in the transversal direction. Considering transverse stress, the zigzag pattern has higher value as starts at higher temperature compared to unidirectional but in case of stress along the length, there is not much difference between the two strategies.

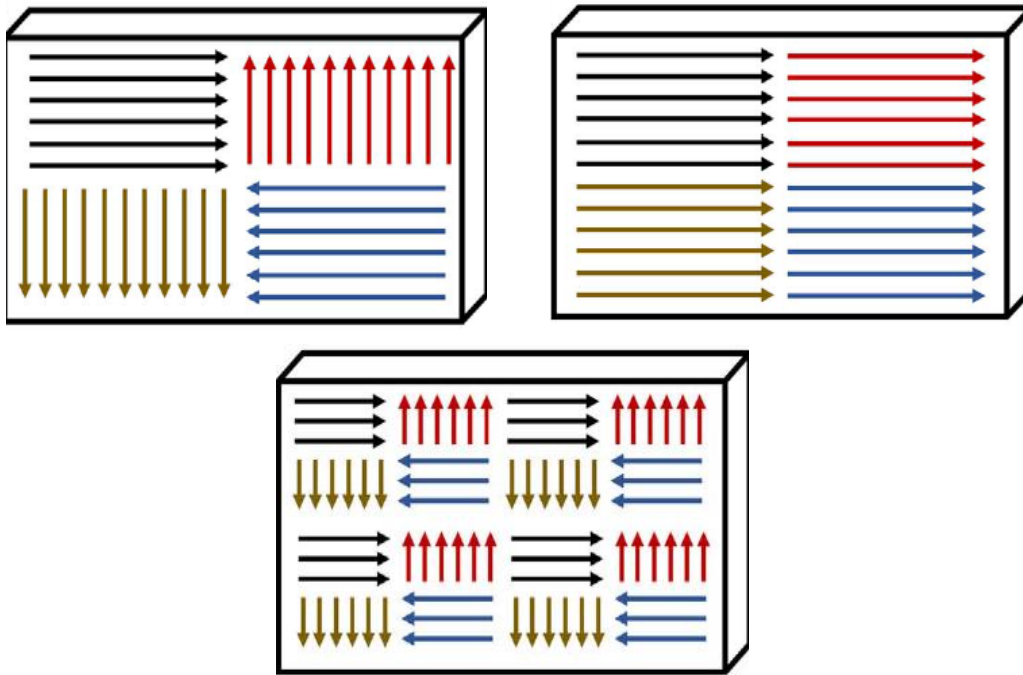


Fig. 1.12 Various patterns of island scanning strategy [30].

Adopting zigzag strategy, after finishing the first laser track, the second track starts at a higher temperature while in the case of unidirectional strategy, the second laser starts its path at a temperature almost equal to the first track. In zigzag strategy the thermal gradient decreases compared to unidirectional strategy. After a few milliseconds of time, the temperature gradient would not change based on the laser scan position. Regarding the strain it would be observed that during zigzag laser scan less consistent plastic deformation achieved as compared to parallel pattern [31],[32].

1.7.1 Hatch Space

Hatch space is defined as the distance between two lasers next to each other in a two-laser track strategy, in other words, it is the distance between centers of two lasers. The hatch space would affect the total time and overall precision for

production of each layer. In the case that the distance between two lasers increases, the amount of time to produce the layer decreases while if the hatch space decreases, the amount of time would increase. Bigger laser beam diameter with higher intensity of laser power is used in the case that the distance between two lasers increases. If not considering big laser beam diameter for increased hatch space, the porosity defect would appear in the final part. Therefore, the value of the hatch space can be increased up to a certain value. As a general rule, the value of the temperature in center of the gaussian laser is higher compared to its surrounding so to decrease the thermal gradient across the laser beam and avoid appearance of the porosity defect on the final workpiece, it is tried to have interference between two subsequent lasers [17]. Lung Lo et al tried to evaluate the impact of parameters such as scan length and hatch space on melt pool during the SLM process of two laser tracks and further optimized hatch space by adopting artificial neural networks to estimate temperature of melt pool, the rate of overlap between two subsequent tracks and depth of melt pool. Accordingly, they found out that the optimal value of hatch space is about 61% of the laser beam diameter where the laser power equals 180W, scanning speed is 680mm/s, and laser beam diameter equals 120 μ m [33].

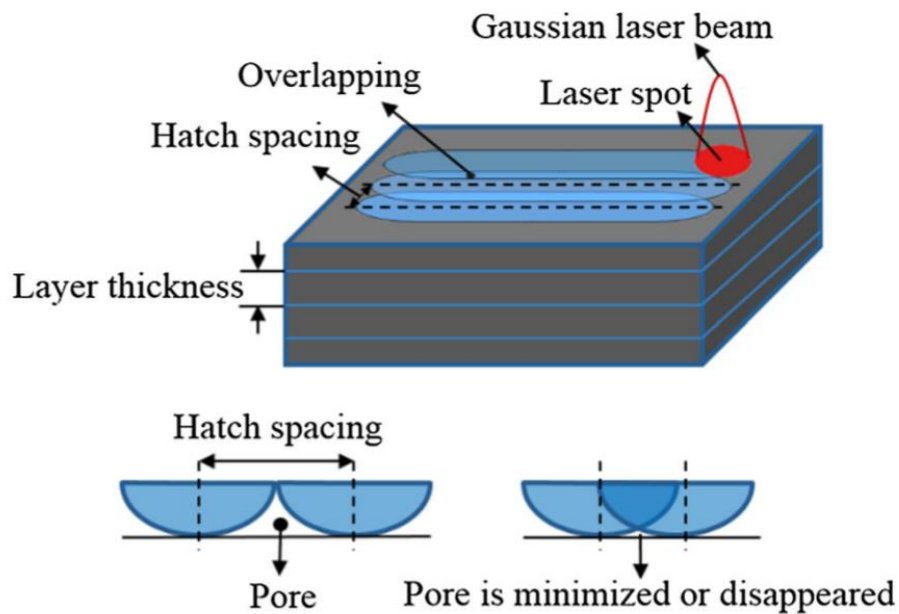


Fig. 1.13 The pattern of hatch space indicating the overlap of two subsequent lasers [34].

1.8 Melt Pool

When the high intensity gaussian laser beam strikes the powder bed, the powder absorbs the laser's heat and gets melted. Marangoni convection which appears due to the gradient in surface tension is the factor of mass transfer within the melt pool. The flow in the pool would move away radially provided that the gradient of surface tension is negative and for positive surface tension the mass of the melt transfers radially. The thermal gradient and maximum temperature in the melt pool rise when the laser beam intensity increases. The melt pool dimension including length, width and depth has direct relation with power intensity. The stability of melt pool defines whether the built-up part has got good quality or not. If the dimension of the melt pool is small, then the final quality is appropriate. When laser beam intensity increases, the dimension of the melt pool increases too, so it is prone to instability. In addition, laser diameter value can play a role in instability, if adopting large laser diameter, then the quality of the surface decreases by the appearance of holes and other defects. Furthermore, too small laser beam diameter can cause evaporation of energy. As a result, choosing the right dimension of the laser spot is of great importance to avoid instability [35].

1.8.1 Laser Beam Size

The right selection of laser beam diameter can lead to the appearance of a stable melt pool. The very small laser beam size increases the possibility of having defect and non-uniform melt pool. The density of workpiece obtained by increase of laser beam size is higher than smaller beam spot diameter. Wentian Shi et al did comparison between two laser beam diameters of 50 μ m and 200 μ m and they found the following values of yield strength and elongation, respectively 1035MPa and 5.91% for smaller laser beam size and 1150 MPa and 8.02% for the bigger spot size. It has been indicated that during high power intensity SLM processes the increase of laser beam size can lead to stability of the built workpiece. Adopting large or small laser beam diameter, by increase of scanning velocity, the track gets rougher as the melting process would not be done completely, which is more

intense in the case of larger beam diameters and in case of exceeding velocity, balling effect and discontinuity appear. Using large laser beam diameters with low scanning velocity, increase the smoothness of the surface. In general, if the laser beam has got a large laser beam diameter, the increase of speed can lead to surface defects while increasing the scanning velocity for the smaller beam size makes no morphological defect. Using small laser beam diameter, the shape of the pool obtained could be like a deep funnel, which is due to the application of high laser intensity with small size of beam which is not recommended since the rate of evaporation increases. Considering the same scanning velocity, the penetration of the melt pool obtained using large laser beam size is less deep. With increasing the scanning velocity, the penetration of the melt pool of large beam diameter decreases since there is less concentration of laser beam intensity on the powder bed, however the possibility of balling defect increases.

Considering the same scanning velocity of laser, the width of the melt pool is not affected by the laser beam diameter. Comparing the variability of the melt pool dimensions for small and large beam diameters with respect to change in scanning velocity, would be apparent that the small beam size is more sensitive which induces more instable melt pool [36,37,38].

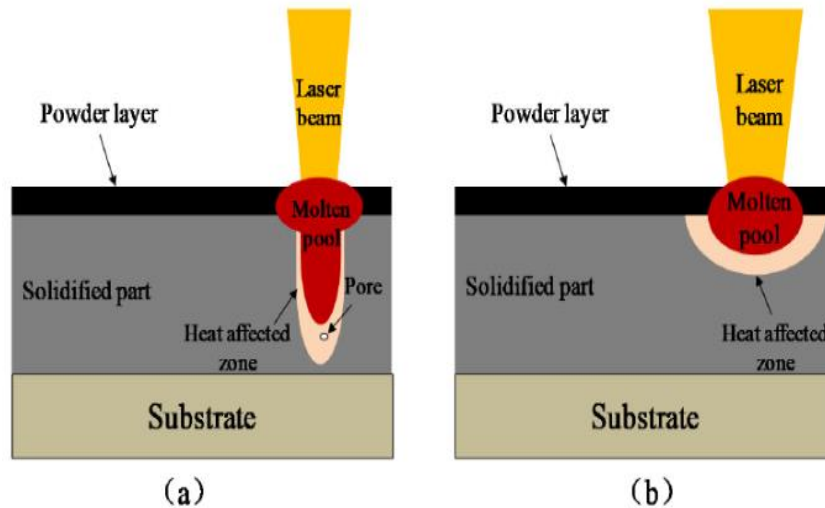


Fig. 1.14 Melt pool configuration of high-density laser for (a) small laser beam diameter and (b) large laser beam diameter [36].

Chapter 2

Model Description

2.1 Heat Transfer Equations

In Selective Laser melting when dealing with heat transfer, should consider three types of heat transfer forms such as heat conduction, heat convection and radiation to account for the heat that is introduced by movement of the laser along the powder bed. In Fig. 2.1, the geometry of substrate and power bed along with available heat transfer forms have been depicted. The heat conduction equation plays the main role in creating the temperature gradient across the powder bed and convection and radiation are considered as heat losses. According to the Fourier's law of heat conduction in three dimensions, we have [39]:

$$\rho \frac{\partial(c_p T)}{\partial t} = \frac{\partial}{\partial x} \left(k \frac{\partial T}{\partial x} \right) + \frac{\partial}{\partial y} \left(k \frac{\partial T}{\partial y} \right) + \frac{\partial}{\partial z} \left(k \frac{\partial T}{\partial z} \right) + Q \quad (1)$$

Where ρ is the density of powder, t is time, c_p is specific heat capacity, k is thermal conductivity of powder and Q stands for volumetric heat generation in the work piece.

Heat convection usually occurs when we have solid and fluid. The equation of heat convection from the powder bed is:

$$q_{conv} = h(T - T_0) \quad (2)$$

Where h is convective heat transfer coefficient equal to 10 in our case and T_0 is the initial temperature which relates to the ambient temperature and in our study is equal to 20 °C.

Equation of heat loss through radiation is written as below:

$$q_{rad} = \varepsilon\sigma(T^4 - T_0^4) \quad (3)$$

In this relation, ε is emissivity of powder equal to 0.35 in our case, σ is the Stefan-Boltzmann constant ($5.67 \times 10^{-8} \text{ W/m}^2\text{K}^4$), T_0 is the initial temperature which indicates the ambient temperature. As represented in Fig. 2.1, when the laser beam moves perpendicularly along y direction on the powder bed, solidification takes place and the part is built.

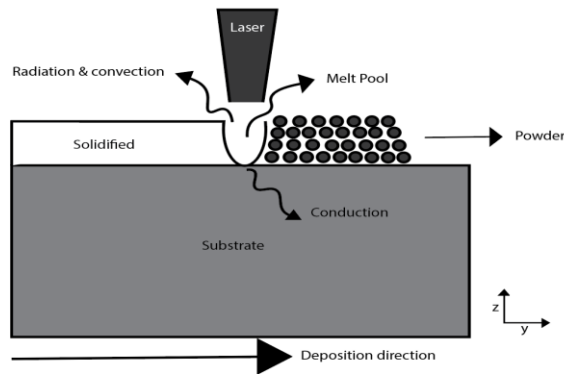


Fig.2.1 Schematic of heat transfer formations during Selective Laser Melting.

2.1.1 Initial & Boundary Conditions

In order to solve the heat differential equation, one should define the auxiliary boundary conditions in the domain. In this way we can get the precise result by specifying temperature, velocity or another variable depending on the configuration. The first condition to be prescribed is initial temperature corresponding to the environment, which is a Dirichlet boundary and is presented as:

$$T(x, y, z, t) = T_0 \quad (4)$$

for $t = 0$

The second boundary condition corresponds to the heat originating from the heat source i.e., the whole laser beam heat source equals the heat fluxes formed by of radiation, conduction, and convection. In this condition, we have Robin boundary condition which is defined as [39]:

$$Q_s = k\nabla T \cdot n + h(T - T_0) + \varepsilon\sigma(T^4 - T_0^4) \quad (5)$$

Q_s is the heat source flux which is presented by Eq.6.

The thermophysical properties of Ti-6Al-4V such as c_p , k , and ε are given in table 1[43].

2.2 Laser Heat Source Model

Different forms of heat sources are used to model the movement of the laser numerically in SLM. The most applicable can be mentioned as Gaussian heat source model, volumetric heat source model, and ellipsoid heat source model [40]. For simulation of the SLM, the gaussian profile is used where there is a high amount of energy in the center of the beam compared to its margins. This high energy is absorbed by the powder depending on the rate of the absorption and the powder gets melted if the temperature is above the melting temperature of the powder. If the energy amount increases, the molten pool dimensions also increase, which can be a source of failures such as balling defect and stress, yet the remaining area stays cool with no change in material strength. On the other hand, if the power density is low, the absorption rate would be lower, therefore it cannot create a thermal gradient inside the powder bed. Due to the existence of surface tension, there would be a flow which moves from the center of the laser beam to its surrounding, the mass transfer in this case is called the Marangoni effect [19]. Laser beam (Q_s) moves along y direction perpendicularly in z direction and is simulated through a gaussian heat profile [41] which is defined as:

$$Q_s = \frac{2PA}{\pi R^2} \exp\left(-\frac{2r^2}{R^2}\right) \quad (6)$$

Where P is the laser power in watt, A is the absorption coefficient of powder when laser strikes the powder and it depends on type of the material where in our case for Ti-6Al-4V powder assume to be same as Ti which is taken as 0.77 according to C. H. Fu et al [42], R indicates the laser beam radius and r denotes the distance between the point on powder bed and laser beam center and it is defined as:

$$r = \sqrt{(x - x_0)^2 + (y - vt - y_0)^2} \quad (7)$$

Where x_0 and y_0 indicate the initial position of the laser on the powder bed in meter and v denotes the scan speed in meter per second along y direction. As the laser beam moves on, the thermal gradient is formed and at hot zones above the melting temperature of Ti-6Al-4V, which is around 1655 °C powder gets melted and afterwards the zone reaches solidification, and the layer is built as long as the laser completes the track along the powder bed.

2.2.1 Numerical Model

ANSYS software, version 18.2 in the space of Transient Thermal analysis system also called workbench is used based on the finite element analysis to simulate the temperature evolution during selective laser melting. The first step taken is to define the material as we have Ti6-4Al-6V [43] properties for the powder and steel properties for the substrate that is taken as default. It is done by opening Engineering Data tab and, accordingly, the material is created with specifying properties such as thermal conductivity, specific heat, and density. As can be seen, the thermal conductivity and specific heat are taken as temperature dependent while density is considered to be constant.

Table 1 Thermal properties of bulk Ti6-4Al-6V [43].

Temperature (K)	Thermal conductivity($W \cdot m^{-1} \cdot K^{-1}$)	Specific heat capacity ($J \cdot K^{-1} \cdot kg^{-1}$)
298	7.0	546
573	10.15	606
973	15.5	694
1268	22.7	753
1268	19.3	641
1573	23.7	696
1923	28.4	759
1923	33.4	831
1973	34.6	840
2500	35.0	850

Table 2 physical properties of bulk Ti6-4Al-6V [43]

Elastic modulus (GPa)	110
Solidus temperature (°C)	1605
Liquidus temperature (°C)	1655
Density (kg/m ³)	4420

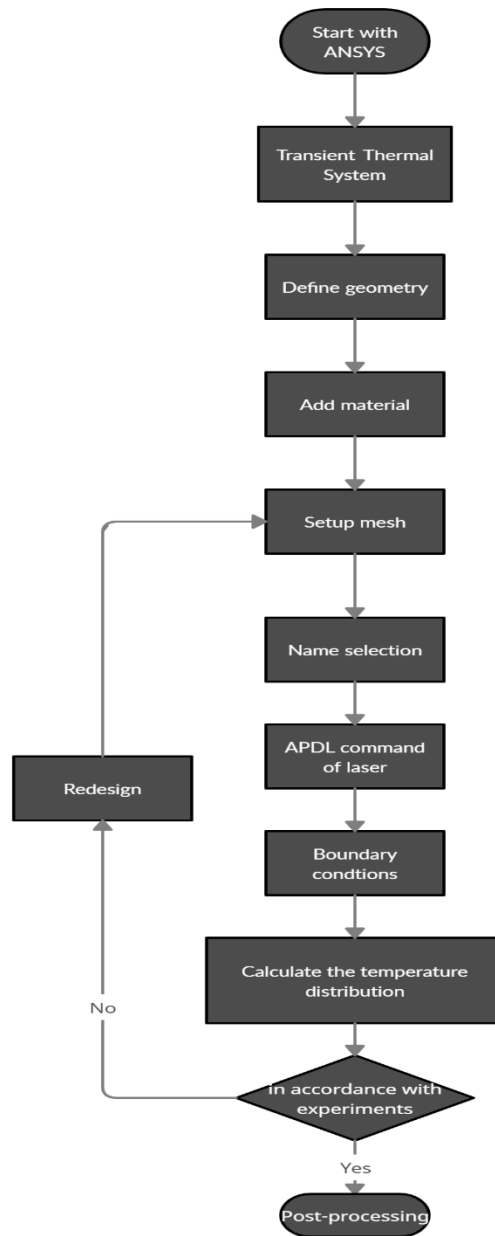


Fig.2.2 Flowchart of SLM process simulation with ANSYS.

The next step includes describing the geometry of steel substrate with dimensions $3\text{mm} \times 3\text{mm} \times 2\text{mm}$ and powder bed geometry of dimensions $2\text{mm} \times 2\text{mm} \times 2\text{mm}$, that is done by opening the geometry tab and selecting Design Modeler. The scan area where the laser beam is going to cover is chosen with $1\text{mm} \times 1\text{mm}$ dimensions. The mentioned dimension of scanning area enables shorter time for completing the simulation as compared to the whole area of the specimen. Then in the next step, open the Model tab. The mesh type is chosen with tetrahedron elements in order to reduce the simulation time fine elements nearly equal to $1.75\text{e-}5\text{mm}$ are considered with hard behavior in the scan area and larger mesh sizes considered in the surrounding and substrate. The geometry of the workpiece along with adopted mesh pattern have been depicted in Fig. 2.2. Mesh statistics report that number of generated elements and nodes is equal to 26296 and 44498, respectively.

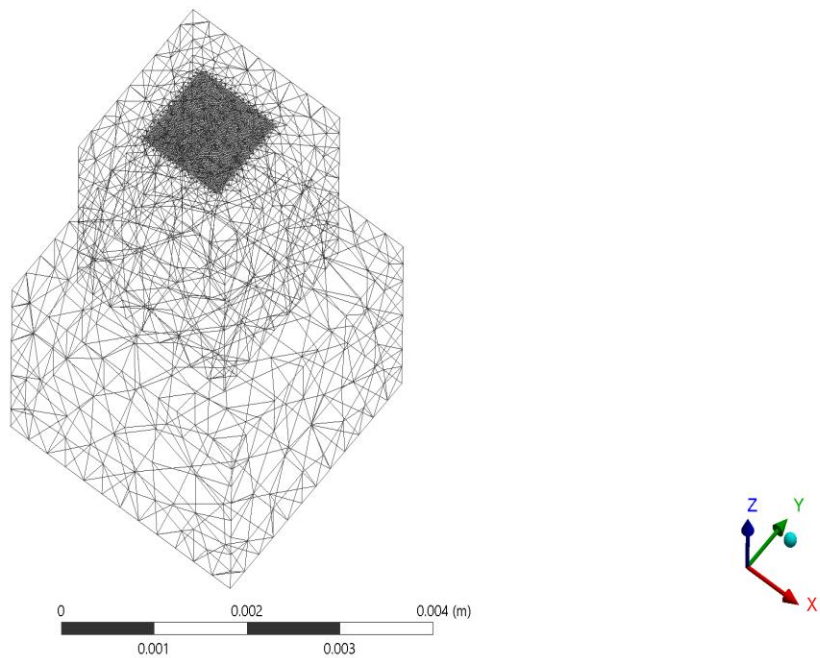


Fig.2.3 Three-dimensional finite element model of workpiece during SLM.

Laser simulation parameters namely power, scan velocity, hatch space, laser incident diameter, ambient temperature have been defined with their respective values in table 3. Accordingly, we will do simulation for two power levels such as 2W and 10W and two different scan speeds including 1mm/s and 10mm/s. The simulation is achieved for two scan strategies which first start with parallel scan tracks and end with zigzag tracks strategy. These strategies have been represented in Fig. 2.3, for these two strategies the distance between each two tracks or better to say hatch space is taken as 0.2mm.

Table 3 Parameters related to numerical finite element model during SLM process.

Power (p)	2W-10W
Scan velocity (v)	1mm/s-10mm/s
Hatch space (l)	0.2mm
Laser incident diameter (D)	5e-5mm
Ambient temperature (T)	20°C

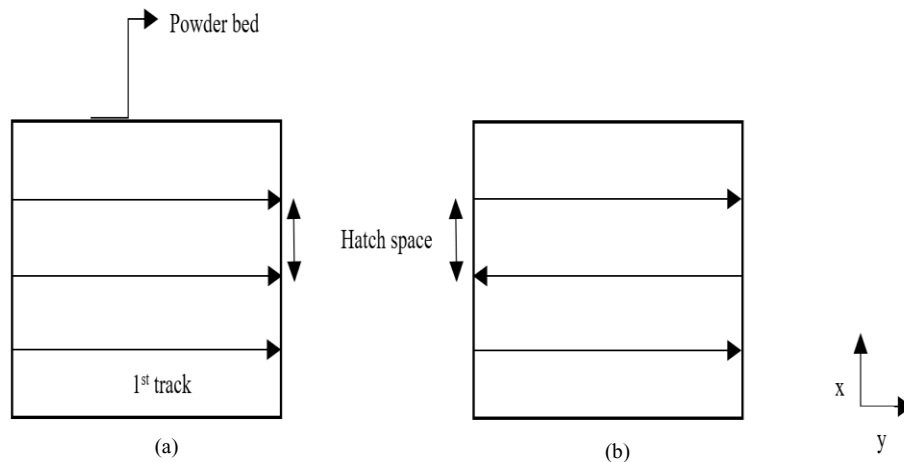


Fig.2.4 Scan strategies in SLM process: (a) parallel - (b) zigzag

Name selection should be done as we have three laser paths, there should be defined three name selections. Our name selections are respectively s1, s2, s3 from left to the right of the workpiece. Name selection should be done, in this way the commands can be related to the proper name selected area. Then the APDL commands containing the gaussian laser profile should be inserted since we have three laser tracks, should introduce three APDL commands. APDL commands are generated by using Mechanical APDL system where in Parameter's tab of function editor section, should define the mathematical function of gaussian heat source. In Ansys Function Editor, set the function to be variable in time. The gaussian heat equation is written and the generated APDL are saved, then copied and inserted for each selected domain name. The command generation process has been shown in Fig. 2.4.

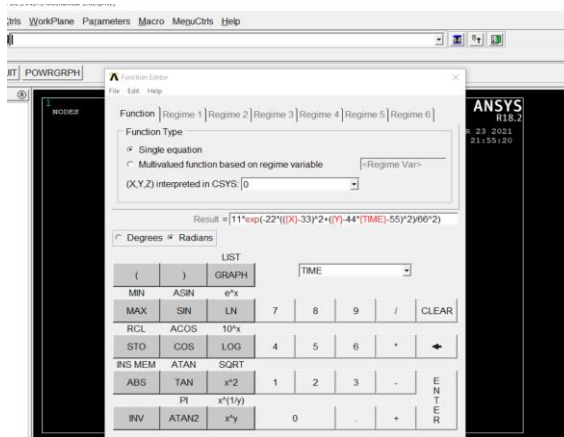


Fig.2.5 Introduction of gaussian laser function to get APDL commands.

In each APDL command the laser parameters such as laser beam radius, scan velocity, laser power and initial positions (x_0 and y_0) of laser beam should be adjusted and for second and third laser scan tracks the time step should be inserted to start the second scan path right after finishing the first scan. The time step is obtained through dividing the scan length by scanning velocity. At the end in analysis setting, specify number of steps and current step number as one and step end time as sum of time for all three laser scans. To start simulation and obtain temperature gradient over the powder bed, right click on solution, and select

temperature, meanwhile, one would check the maximum temperature on solution information. After creating the commands, the radiation and convection boundary conditions should be defined on the part where radiation with defined emissivity is input on the scan area domain and the remaining boundaries are assigned with convection boundary condition.

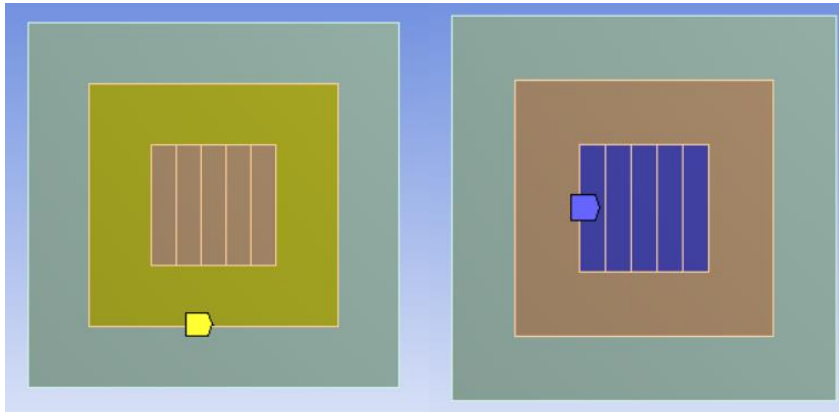


Fig. 2.6 Convection boundary has been defined with yellow color and radiation as blue

At the end, by right clicking on the solution and choosing the temperature, one can obtain the thermal distribution along the scan area. To finalize the simulation and specify the time to finish the laser movement, the sum of each laser scan time should be inserted in step end time inside the analysis setting.

2.3 Experimental methodology

Powder bed of titanium alloy Ti6Al4V would be located in the SLM printer with typical chemical composition and powder size. A thermal camera with high resolution and frame rate is used to measure the thermal distribution across the powder bed and molten area. The camera is focused on the domain where the scanning is done across the laser tracks. The configuration of the camera with respect to the powder bed has been represented in the figure where the powder bed is kept inside a chamber filled with inert gas [44].

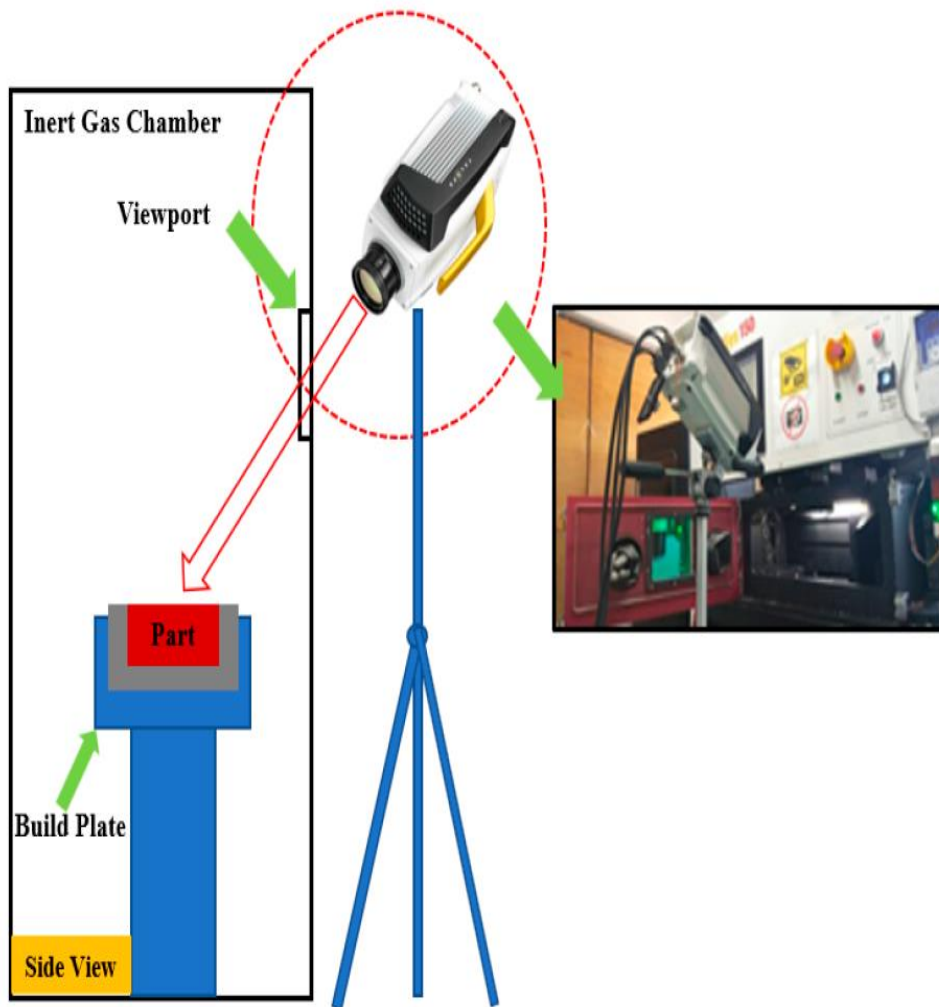


Fig. 2.7 Schematic of experimental Setup [44].

In order to validate the simulated model, results should be compared with experimental ones. The work done by S. Kolossov et al [12] is considered as reference. In the experiment, $5\text{mm} \times 5\text{mm} \times 2\text{mm}$ layer of titanium powder and scan area of dimensions $2\text{mm} \times 2\text{mm}$ were considered. The space between each track of the laser set to 0.1mm . Laser parameters according to S. Kolossov et al are given in table 2. In the experiment, Raytheon infra-red camera has been placed at position $x=1.85\text{mm}$ and $y=2.5\text{mm}$ to record temperature on top surface. The obtained results are shown in Fig. 2.7. The maximum temperature filmed by camera is around 2500°C .

Table 4 Laser characteristics by Kolossov et al[45]

Power (p)	2W
Scan velocity (v)	1mm/s
Laser incident diameter (R)	$2.5\text{e-}5\text{mm}$

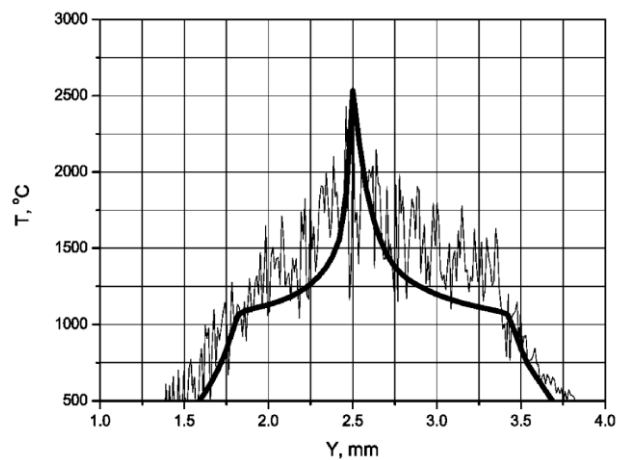


Fig.2.8 Experimental thermal distribution by Kolossov et al at $X= 1.85, Z= 2.0$ [45]

The simulated model has been applied to the geometry described by S. Kolosov et al and titanium properties such as thermal conductivity and specific has been derived from handbook [46]. The maximum temperature is obtained at around $y=2.5\text{mm}$ at $z=2\text{mm}$ which is equal to $2060\text{ }^{\circ}\text{C}$ with 17% error. The comparison of experimental and simulated results has been depicted in Fig. 2.9.

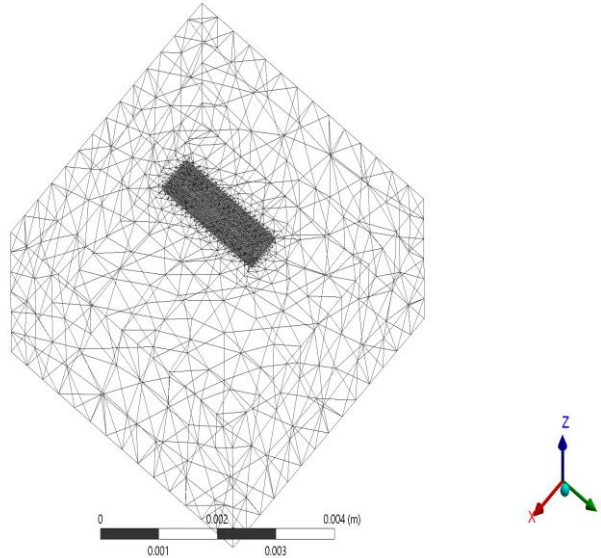


Fig.2.9 Mesh developed for simulating experimental work done by S. Kolosov et al [46]

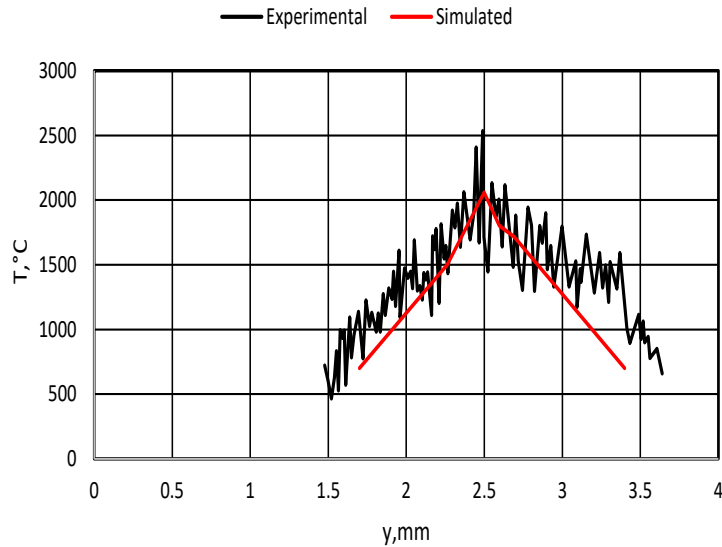


Fig.2.10 Comparison of simulated result obtained for experimental work done by S. Kolosov et al [46].

The next validation took place with simulated results obtained by Yali Lia et al [47] where he considered Ti powder bed with a length of 2.0 mm and a width of 1.0 mm and substrate for the powder bed of a block of C45 medium-carbon steel with dimensions of 3 mm × 1.8 mm × 0.3 mm. The simulation parameters were as laser spot size diameter=0.1mm, scan speed=100mm/s and laser power=100W. At the end of the first scan track (Fig. 2.10) at $t = 18.50$ ms, the predicted maximum temperature of the powder bed was 1929°C while the results obtained by our model oscillates around 2000°C.

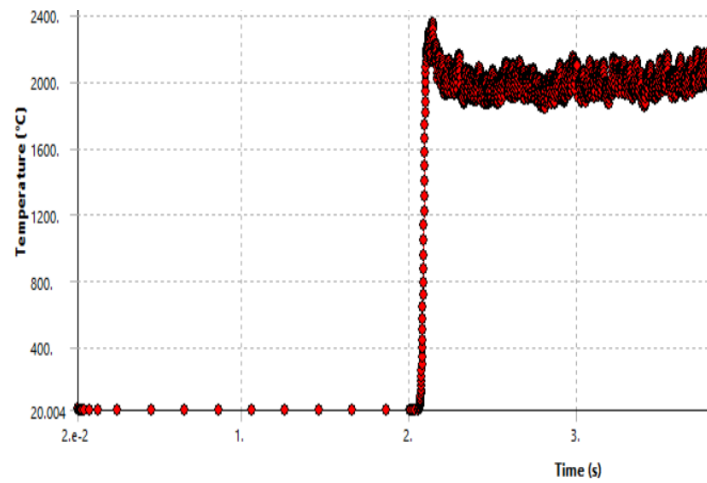


Fig. 2.11 The temperature at the end of 1st scan track is around 2000°C

Chapter 3

Results

3.1 Scan strategy

Thermal distribution of first, second and third scan tracks with parallel strategy has been obtained for power level 2W for scan speed of 10mm/s to see the maximum temperature reached on the top face of workpiece. The maximum temperature reached during the first scan path for 2W is about 1486°C at 0.073 second after simulation. While the maximum temperature reached for second laser track which moves at the center of workpiece is around 1484°C at 0.187 second after simulation. The maximum temperature obtained for the third track is around 1508.6°C. The increase in thermal distribution is attributed to the heat accumulation by previous track. The maximum thermal distribution on the powder bed for all the tracks has been depicted in Fig. 3.1. After each scan reaches the end of track the work piece cools down to around 300°C and then the next scan starts moving.

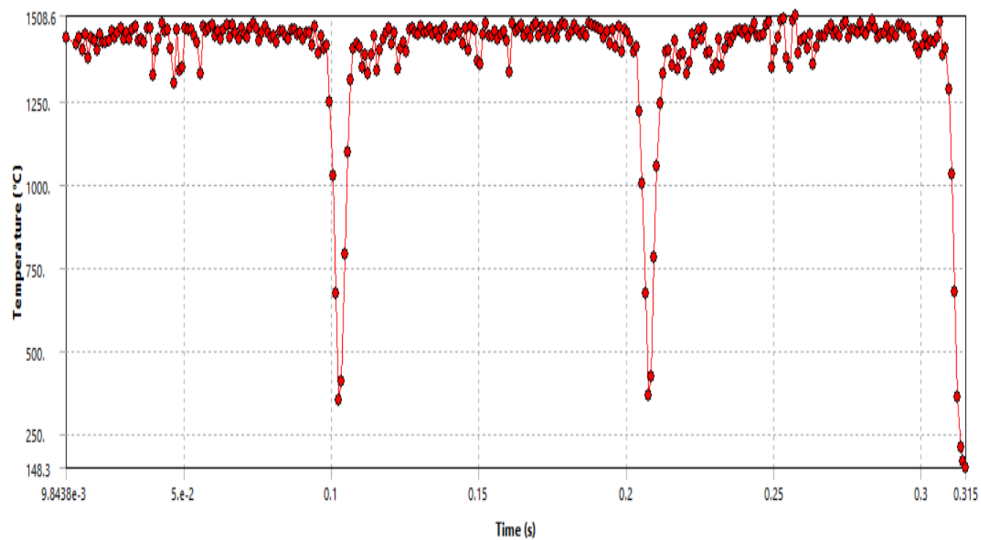


Fig.3.1 Temperature distribution of first, second and third laser scan tracks adopting parallel strategy at velocity of 10mm/s for $p=2W$.

By adopting the zigzag strategy with the same scan velocity of 10mm/s and power level of $p=2W$, the thermal distribution has been investigated. The maximum temperature obtained for the first scan track is about $1486^{\circ}C$ at 0.073 second during simulation. For the second laser track the maximum temperature of $1496^{\circ}C$ obtained at 0.183 second after starting the simulation. The last track reached temperature of $1508.7^{\circ}C$ at 0.257 second after the simulation. The max temperature profile across the three laser tracks has been represented in Fig. 3.2. As can be seen there is not any significant difference among the zigzag and parallel strategies for power level of $p=2W$ however the temperature profile across the second laser track increases.

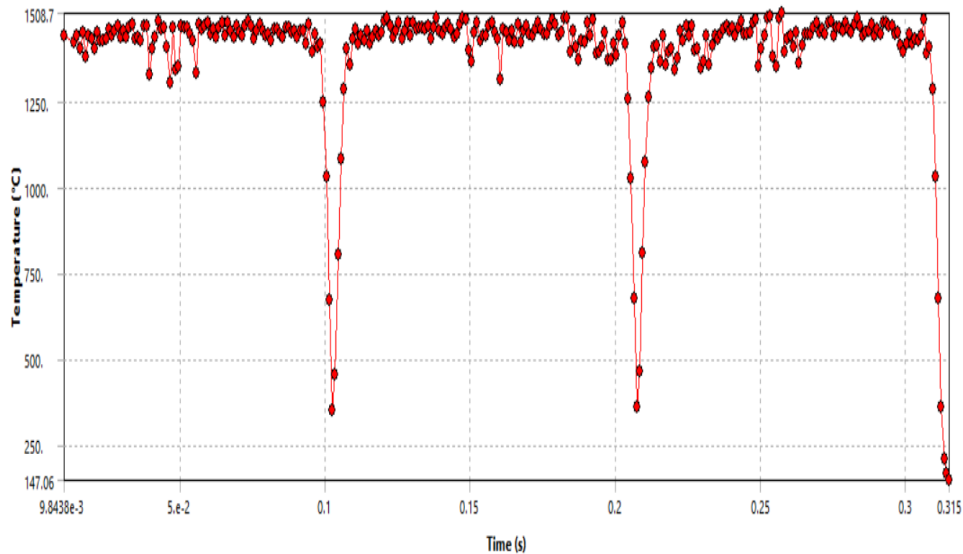


Fig.3.2 Temperature distribution of first, second and third laser scan tracks adopting zigzag strategy at velocity of 10mm/s for $p=2W$

By increasing power level from $p=2W$ to $p=10W$ with the same laser scan velocity of 10mm/s in the form parallel, the thermal profile according to Fig. 3.3 is obtained.

The maximum temperature obtained at the power of 10W is about 4127.7°C when 0.253 second passed. The maximum temperature for first and second laser tracks are 4075°C and 4081°C respectively.

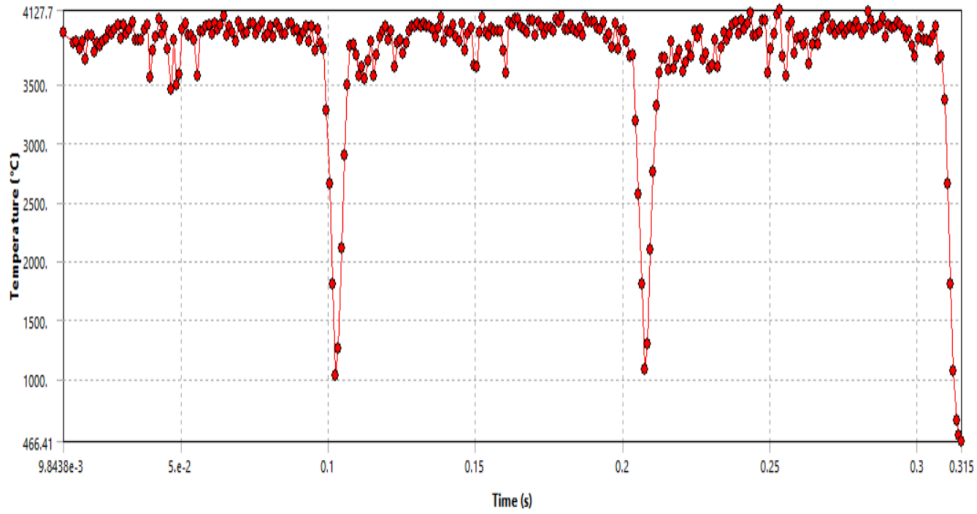


Fig.3.3 Temperature distribution of first, second and third laser scan tracks adopting parallel strategy at velocity of 10mm/s for p=10W.

By altering the configuration to zigzag the maximum temperature obtained on the powder is around 4128°C which is higher than the maximum temperature obtained for the parallel strategy, however not significant which can be related to the small dimensions of scan area which 1mm×1mm.

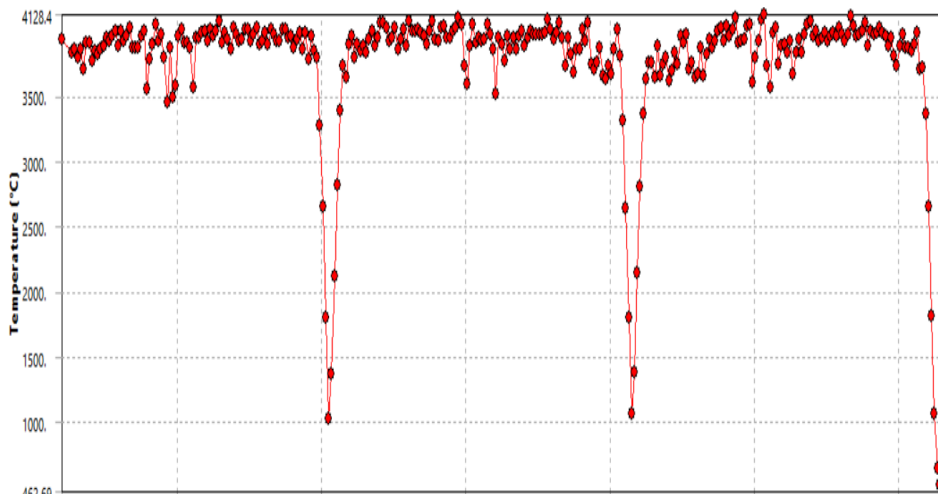


Fig.3.4 Temperature distribution of first, second and third laser scan tracks adopting zigzag strategy at velocity of 10mm/s for p=10W

The time history of laser temperature profile across the powder bed for various power levels and scanning velocity has been depicted.

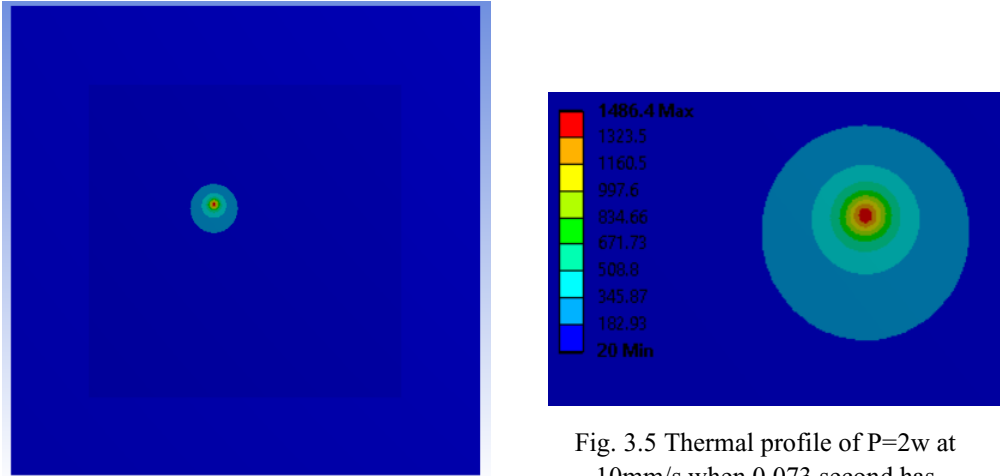


Fig. 3.5 Thermal profile of P=2w at 10mm/s when 0.073 second has passed during SLM process.

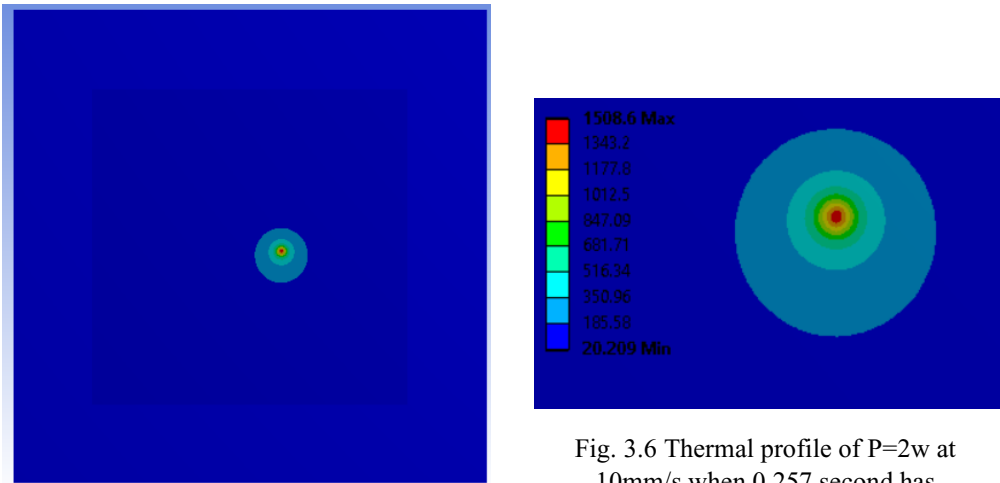


Fig. 3.6 Thermal profile of P=2w at 10mm/s when 0.257 second has passed during SLM process.

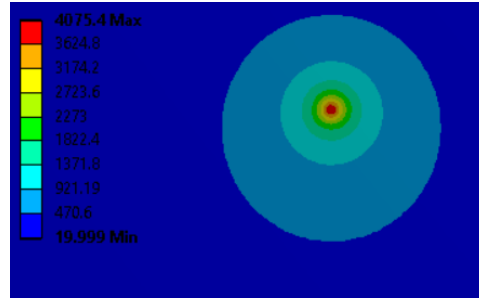
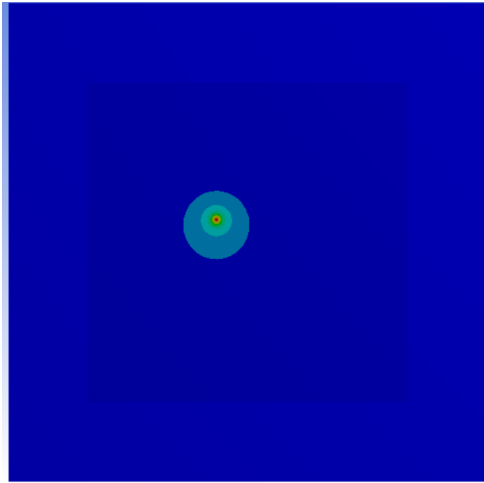


Fig. 3.7 Thermal profile of P=10w at 10mm/s when 0.0643 second has passed during SLM process.

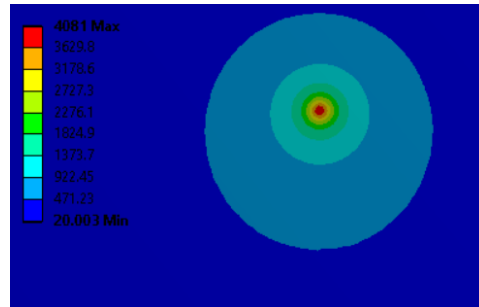
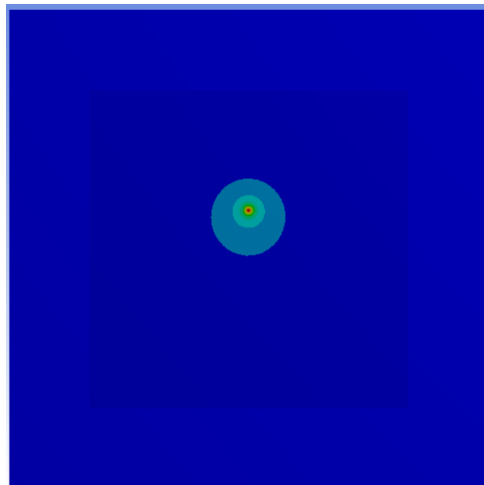


Fig. 3.8 Thermal profile of P=10w at 10mm/s when 0.179 second has passed during SLM process.

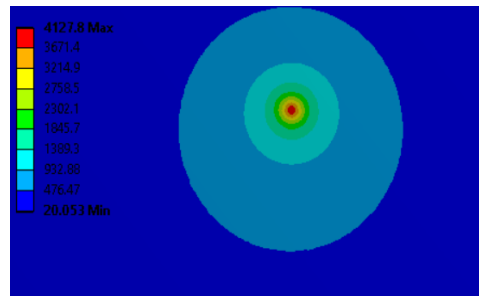
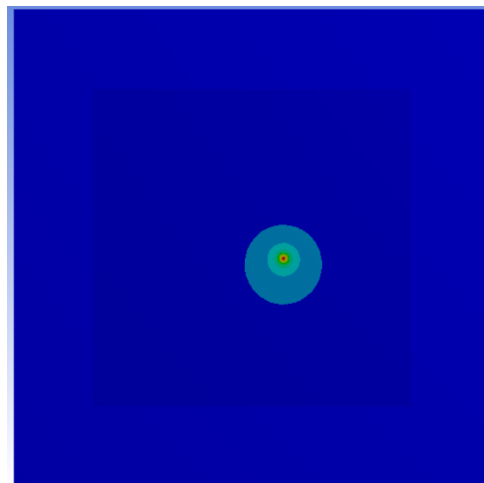


Fig. 3.9 Thermal profile of P=10w at 10mm/s when 0.253 second has passed during SLM process.

3.2 Power effect

During SLM process, in order to understand the effect of laser beam power on thermal distribution, two levels of laser power respectively 2 and 10 W are applied with the fixed scan velocity of 1mm/s according to the parallel scan strategy. The maximum temperature obtained for $p=2W$ is around $1535^{\circ}C$ across the third laser track when 2.57 second has passed.

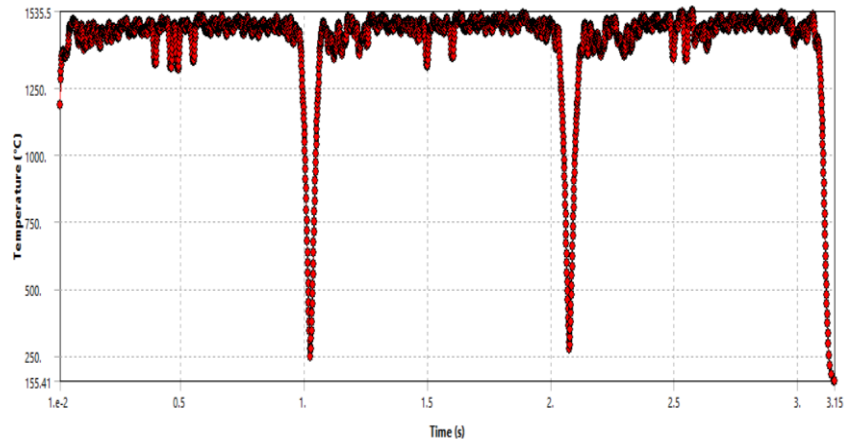


Fig.3.10 Temperature distribution of first, second and third laser scan tracks adopting parallel strategy at velocity of 1mm/s for $p=2W$.

With increasing power to $p=10W$, the maximum temperature across the third laser track reaches $4234^{\circ}C$.

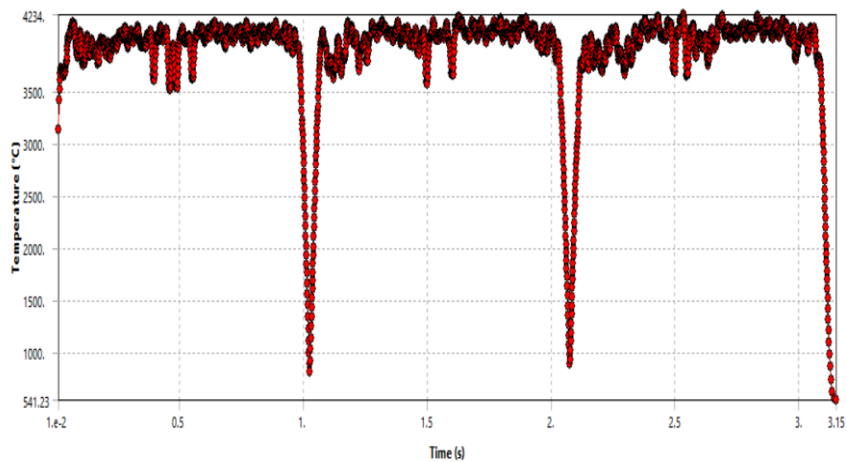


Fig.3.11 Temperature distribution of first, second and third laser scan tracks adopting parallel strategy at velocity of 1mm/s for $p=10W$.

As can be seen the temperature along the path of laser scan is lower for $p=2W$ while with increasing power to $p=10W$ the thermal gradient rises along y direction. In addition, the length of laser profile on powder bed increases when the power rises from 2 to 10 watt. The melt pool dimensions of power $p=10W$ has been represented in terms of length and depth however the possibility to formation of melt pool for $p=2W$ is low according to the thermal distribution as the melting temperature of Ti-6Al-4V is around $1655\text{ }^{\circ}\text{C}$.

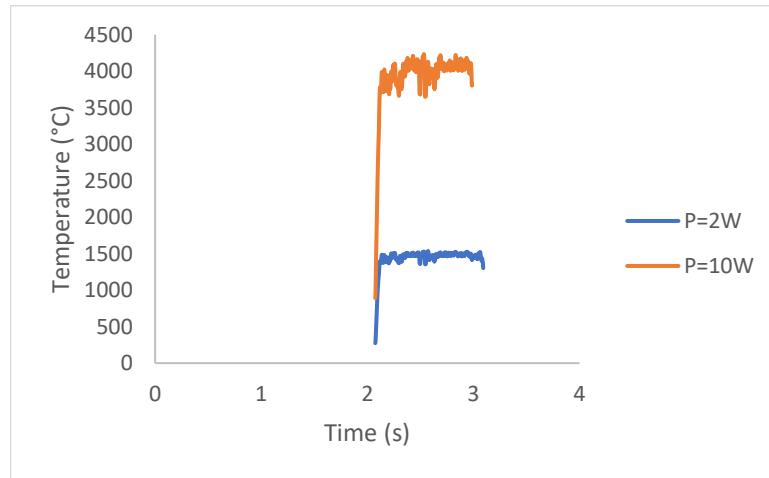


Fig. 3.12 Maximum temperature distribution across the third laser track for power of 2 and 10 watt.

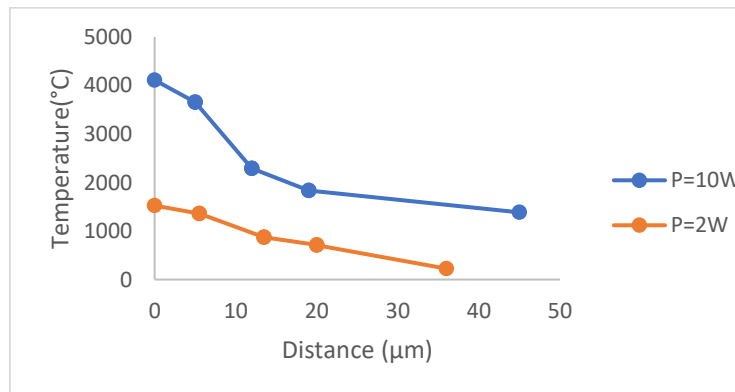


Fig. 3.13 Temperature gradient of laser heat source along scan direction from center of laser.

3.3 Scanning velocity effect

In order to understand the effect of laser scanning velocity and compare it with laser power effect, the scan velocity is increased from 1mm/s to 10mm/s for the power level of 2 watt furthermore the power level of 10 watt is used to investigate the melt pool dimensions formed. The maximum temperature obtained for $p=10\text{W}$ at 1mm/s as represented before is 4234°C while at 10mm/s the maximum temperature is 4127°C therefore by increasing the scan velocity the maximum temperature decreases. As can be seen the order of the thermal distribution increase by power rise is larger than scan laser velocity.

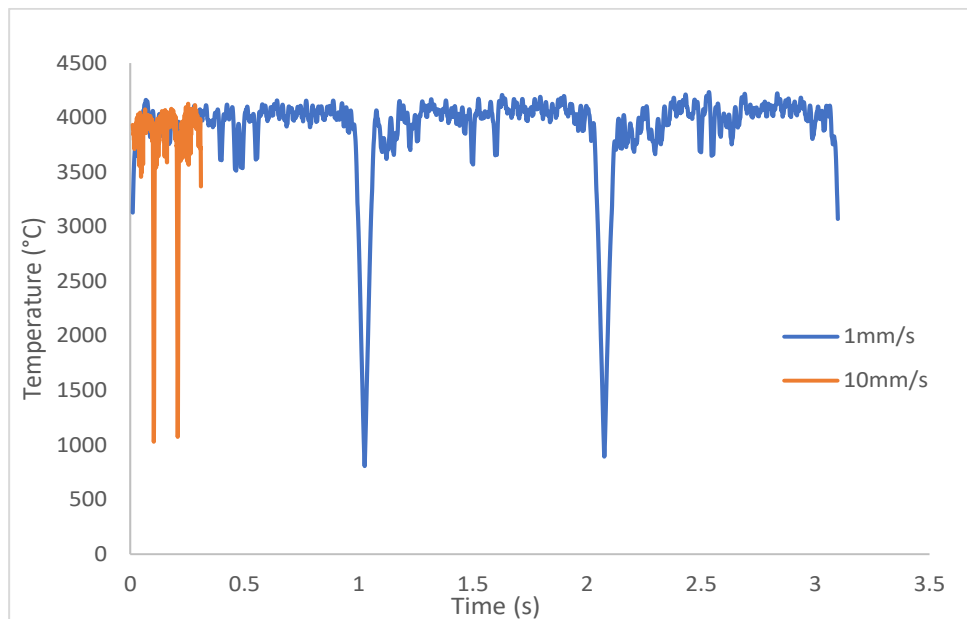


Fig. 3.14 Temperature profile of power at 10 watt for two scan velocity of 1 and 10mm/s across time

By increasing the scan velocity from 1 to 10mm/s of 10 watt power, the length and depth of molten pool decrease from 78 μm and 40 μm to 63 μm and 32 μm respectively. The dimensions of molten pool have been shown in the Fig. 3.15.

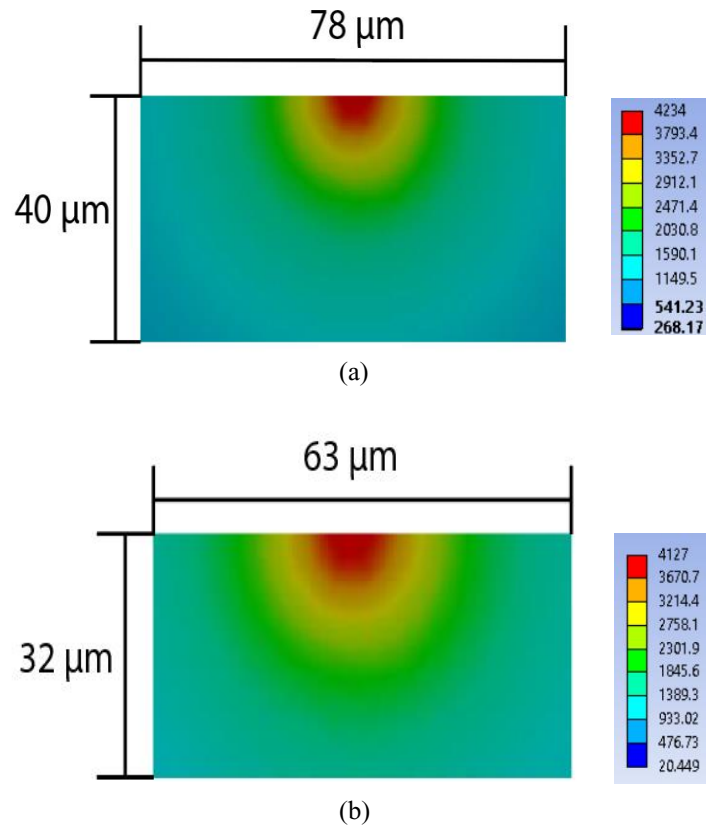


Fig. 3.15 Melt pool dimensions including length and depth at power level of 10W for (a) : 1mm/s and (b) : 10mm/s

3.4 Residual stress

To evaluate the amount of stress formed during the SLM process, should couple the transient thermal analysis system to transient structural where the model and solution of thermal system is linked to model and setup of transient structural system.

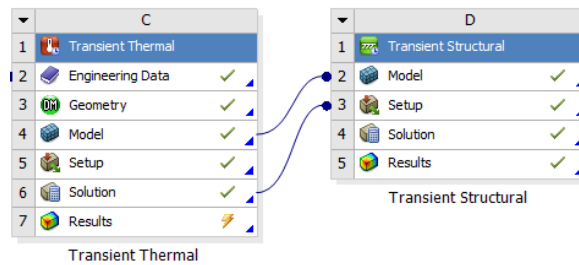
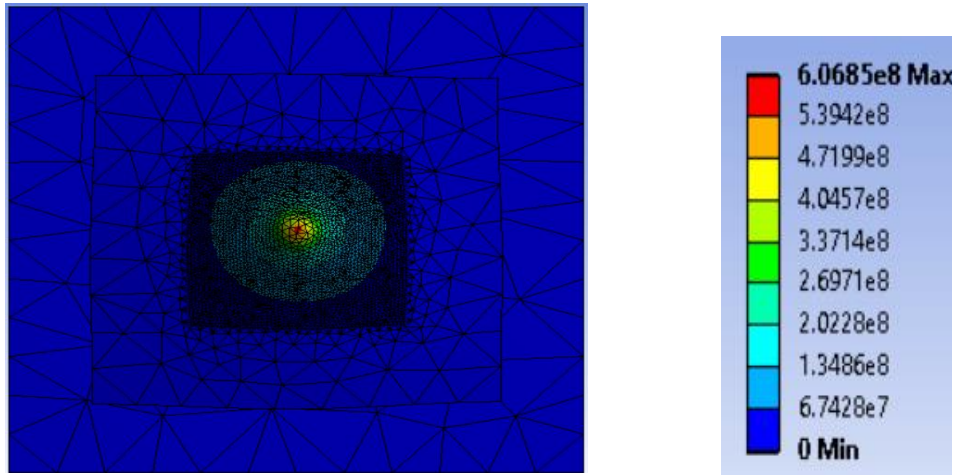


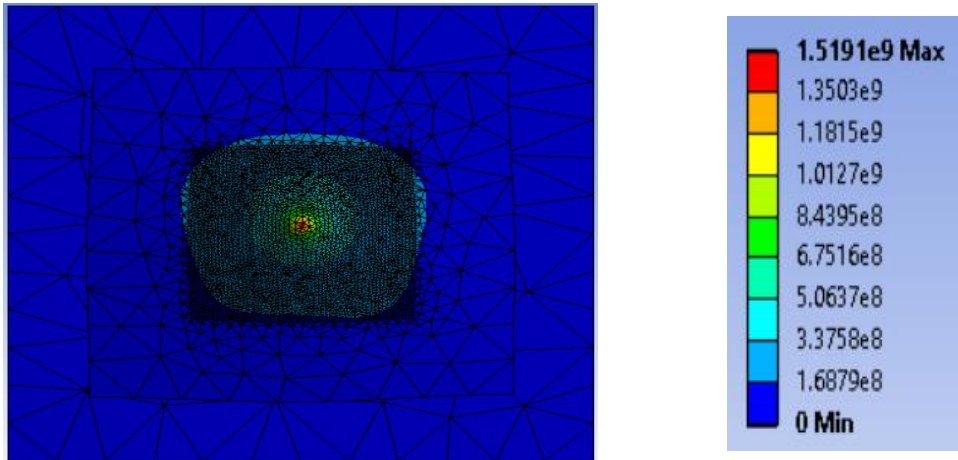
Fig. 3.16 Schematic of coupling of thermal and structural system.

In the analysis settings set the base as fixed support and define the values of initial time step, step end time, minimum and maximum time step. Then click on the imported body temperature, set the source time as all, and right click to import the temperature loads. To investigate the residual stress, one should choose the equivalent von mises stress and start the analysis.

The maximum stress obtained during SLM process when the power level of 2 watt with scan velocity of 10mm/s was adopted is around $6e8$ pa while the equivalent von mises stress obtained for power of 10 watt at 10mm/s scan velocity is around $1.5E9$ pa.



(a)



(b)

Fig 3.17 Equivalent Von mises stress profile for (a) : p=2w and scan velocity of 10mm/s , (b) : : p=10w and scan velocity of 10mm/s

References

- [1] Chunze Yan, Yusheng Shi, Li Zhaoqing, Shifeng Wen, Qingsong Wei. Selective Laser Sintering Additive Manufacturing Technology, 2020.
- [2] Abbas Razavykia, , Eugenio Brusa, Cristiana Delprete and Reza Yavari. An Overview of Additive Manufacturing Technologies—A Review to Technical Synthesis in Numerical Study of Selective Laser Melting. <https://doi.org/10.3390/ma13173895>, 2020.
- [3] Razavykia, A., Brusa, E., Ghodsieh, S. and Giorio, L., 2021. DoE Applied to Thermal Analysis and Simulation of Geometrical Stability of a Wind Turbine Blade Made by Selective Laser Melting. In Advanced Materials Research (Vol. 1161, pp. 65-74). Trans Tech Publications Ltd.
- [4] Yang, L., Hsu, K., Baughman, B., Godfrey, D., Medina, F., Menon, M., Wiener, S. Additive Manufacturing of Metals: The Technology, Materials, Design and Production, 2017.
- [5] Ian Gibson, David W. Rosen, Brent Stucker. Additive Manufacturing Technologies: 3D Printing, Rapid Prototyping, and Direct Digital Manufacturing, 2014.
- [6] Amit Bandyopadhyay, Susmita Bose. Additive Manufacturing. ISBN: 9781482223606, 1482223600, 2015.
- [7] Yi Zhang, William Jarosinski, Yeon-GilJung, Jing Zhang. Additive manufacturing processes and equipment. <https://doi.org/10.1016/B978-0-12-812155-9.00002-5> , 2018.
- [8] Y. Hagedorn. Laser additive manufacturing of ceramic components: materials, processes, and mechanisms. <https://doi.org/10.1016/B978-0-08-100433-3.00006-3> , 2017.
- [9] Ester M.Palmero, Alberto Bollero. 3D and 4D Printing of Functional and Smart Composite Materials. <https://doi.org/10.1016/B978-0-12-819724-0.00008-2> , 2021.
- [10] Sing, S. L., Tey, C. F., Tan, J. H. K., Huang, S., & Yeong, W. Y. 3D printing of metals in rapid prototyping of biomaterials: Techniques in additive manufacturing. <https://doi.org/10.1016/B978-0-08-102663-2.00002-2> , 2020.

- [11] Prashanth Konda Gokuldoss, Sri Kolla, and Jürgen Eckert, Additive Manufacturing Processes: Selective Laser Melting, Electron Beam Melting and Binder Jetting—Selection Guidelines. <https://doi.org/10.3390/ma10060672> , 2017.
- [12] Xu Song, Wei Zhai, Rui Huang, Jin Fu, Mingwang Fu, Feng Li. Metal-Based 3D-Printed Micro Parts & Structures. <https://doi.org/10.1016/B978-0-12-819726-4.00009-0>, 2020.
- [13] Balasubramanian Nagarajan, Zhiheng Hu, Xu Song, Wei Zhai, Jun Wei. Development of Micro Selective Laser Melting: The State of the Art and Future Perspectives, <https://doi.org/10.1016/j.eng.2019.07.002>, 2019.
- [14] Namatollahi, M., Jahadakbar, A., Mahtabi, M. J., & Elahinia, M. Additive manufacturing (AM). Metals for Biomedical Devices, 331–353. <https://doi.org/10.1016/B978-0-08-102666-3.00012-2> , 2019.
- [15] Gokuldoss, P. K., Kolla, S., & Eckert, J. Additive Manufacturing Processes: Selective Laser Melting, Electron Beam Melting and Binder Jetting—Selection Guidelines. *Materials*, 10(6), 672. <https://doi.org/10.3390/ma10060672> , 2017.
- [16] Mohammad Elahinia, Francesco Stortiero. Shape Memory Alloy Engineering (Second Edition) For Aerospace, Structural, and Biomedical Applications. Chapter 6 - Manufacturing of shape memory alloys. <https://doi.org/10.1016/B978-0-12-819264-1.00006-6> , 2021.
- [17] S.Kumar . Selective Laser Sintering/Melting. <https://doi.org/10.1016/B978-0-08-096532-1.01003-7> , 2014.
- [18] Gianni Nicoletto. Efficient determination of influence factors in fatigue of additive manufactured metals, <https://doi.org/10.1016/j.prostr.2017.12.020> , 2018.
- [19] Song Bo, Shifeng Wen, Chunze Yan, Qingsong Wei, Yusheng Shi. Selective Laser Melting for Metal and Metal Matrix Composites, 2020.
- [20] Mostafa Yakout, M.A. Elbestaw, Liping Wang, Richard Muizelaar. Selective laser melting of soft magnetic alloys for automotive applications, Joint Special Interest Group meeting between euspen and ASPE Advancing Precision in Additive Manufacturing Ecole Centrale de Nantes, 2019.
- [21] Uhlmann, E., Kersting, R., Klein, T. B., Cruz, M. F., & Borille, A. V. Additive Manufacturing of Titanium Alloy for Aircraft Components. *Procedia CIRP*, 35, 55–60. <https://doi.org/10.1016/j.procir.2015.08.061> , 2017.

- [22] Munir, K., Biesiekierski, A., Wen, C., & Li, Y. Selective laser melting in biomedical manufacturing. *Metallic Biomaterials Processing and Medical Device Manufacturing*, <https://doi.org/10.1016/B978-0-08-102965-7.00007-2> , 2020.
- [23] Yap, C. Y., Chua, C. K., Dong, Z. L., Liu, Z. H., Zhang, D. Q., Loh, L. E., & Sing, S. L. Review of selective laser melting: Materials and applications. *Applied Physics Reviews*, <https://doi.org/10.1063/1.4935926> , 2015.
- [24] Christoph Leyens, Manfred Peters. *Titanium and Titanium Alloys: Fundamentals and Applications*, Germany: Wiley, 2006.
- [25] Dadbakhsh, S., Mertens, R., Hao, L., Van Humbeeck, J., & Kruth, J.-P. Selective Laser Melting to Manufacture “In Situ” Metal Matrix Composites: A Review. *Advanced Engineering Materials*, <https://doi.org/10.1002/adem.201801244> , 2019.
- [26] Mohammed Alsaddah, Ashfaq Khan, Kristian Groom and Kamran Mumtaz. Use of 450-808 nm diode lasers for efficient energy absorption during powder bed fusion of Ti6Al4V, <https://doi.org/10.1007/s00170-021-06774-4> , 2021.
- [27] Martin Frkan, Radomila Konecna, Gianni Nicoletto, Ludvik Kunz. Microstructure and fatigue performance of SLM-fabricated Ti6Al4V alloy after different stress-relief heat treatments, <https://doi.org/10.1016/j.trpro.2019.07.005> , 2019.
- [28] Haider Ali, Le Ma, Hassan Ghadbeigi, Kamran Mumtaz. In-situ residual stress reduction, martensitic decomposition, and mechanical properties enhancement through high temperature powder bed pre-heating of Selective Laser Melted Ti6Al4V, <https://doi.org/10.1016/j.msea.2017.04.033> , 2017.
- [29] Sufiiarov, V. S., Popovich, A. A., Borisov, E. V., Polozov, I. A., Masaylo, D. V., & Orlov, A. V. The Effect of Layer Thickness at Selective Laser Melting. *Procedia Engineering*, 174, 126–134, <https://doi.org/10.1016/j.proeng.2017.01.179> , 2017.
- [30] Mohammad Masoomi, Scott M. Thompson, Nima Shamsaei Laser powder bed fusion of Ti-6Al-4V parts: Thermal modeling and mechanical implications, <https://doi.org/10.1016/j.ijmachtools.2017.04.007> , 2017.
- [31] L. Parry, I.A. Ashcroft , R.D. Wildman. Understanding the effect of laser scan strategy on residual stress in selective laser melting through thermo-mechanical simulation, <https://doi.org/10.1016/j.addma.2016.05.014> , 2016

- [32] Haolin Jia, Hua Sun, Hongze Wang, Yi Wu & Haowei Wang Scanning strategy in selective laser melting (SLM): a review, <https://doi.org/10.1007/s00170-021-06810-3> , 2021.
- [33] Lo, Y.-L., Liu, B.-Y., & Tran, H.-C. Optimized hatch space selection in double-scanning track selective laser melting process. The International Journal of Advanced Manufacturing Technology, <https://doi.org/10.1007/s00170-019-04456-w>, 2019.
- [34] Pei, W., Zhengying, W., Zhen, C., Junfeng, L., Shuzhe, Z., & Jun, D. Numerical simulation and parametric analysis of selective laser melting process of AlSi10Mg powder. <https://doi.org/10.1007/s00339-017-1143-7> , 2017.
- [35] Pengpeng Yuan, Dongdong Gu. Molten pool behavior and its physical mechanism during selective laser melting of TiC/AlSi10Mg nanocomposites: simulation and experiments, <https://doi.org/10.1088/0022-3727/48/3/035303>, 2015.
- [36] Shi, W., Liu, Y., Shi, X., Hou, Y., Wang, P., & Song, G. Beam Diameter Dependence of Performance in Thick-Layer and High-Power Selective Laser Melting of Ti-6Al-4V. *Materials*, 11(7), 1237, <https://doi.org/10.3390/ma11071237> , 2018.
- [37] Schleifenbaum, H.; Meiners, W.; Wissenbach, K.; Hinke, C. Individualized production by means of high-power Selective Laser Melting. *CIRP J. Manuf. Sci. Technol.* 2010,2, 161–169. <https://doi.org/10.1016/j.cirpj.2010.03.005> , 2010.
- [38] Buchbinder, D.; Meiners, W.; Pirch, N.; Wissenbach, K.; Schrage, J. Investigation on reducing distortion by preheating during manufacture of aluminum components using selective laser melting. *J. Laser Appl.* 2014,26, 012004. <https://doi.org/10.2351/1.4828755> , 2014.
- [39] Adriano Sciacovelli , Vittorio Verda , Romano Borchiellini. *Numerical Design of Thermal Systems*, 2013.
- [40] Ashish Kumar Mishra, Akash Aggarwal, Arvind Kumar, Niraj Sinha. Identification of a suitable volumetric heat source for modelling of selective laser melting of Ti6Al4V powder using numerical and experimental validation approach. <https://doi.org/10.1007/s00170-018-2631-4> , 2018.

- [41] Labudovic M, Hu D, Kovacevic R. A three-dimensional model for direct laser metal powder deposition and rapid prototyping. <https://doi.org/10.1023/A:1021153513925> , 2003.
- [42] C. H. Fu, Y. B. Guo. Three-Dimensional Temperature Gradient Mechanism in Selective Laser Melting of Ti-6Al-4V, <https://doi.org/10.1115/1.4028539>, 2014.
- [43] XING Xiaodong¹, ZHOU Qiuyu¹, WANG Shiyuan¹, WANG Liquan¹, JIANG Fengchun. Numerical Investigation of Transient Temperature Distribution during Ti-6Al-4V Selective Laser Melting, <https://doi.org/10.1007/s11630-019-1082-z>, 2019.
- [44] Md Jonaet Ansari , Dinh-Son Nguyen and Hong Seok Park. Investigation of SLM Process in Terms of Temperature Distribution and Melting Pool Size: Modeling and Experimental Approaches. <https://doi.org/10.3390/ma12081272> , 2019.
- [45] S. Kolossov, E. Boillat, R. Glardon, P. Fischer, M. Locher. 3D FE simulation for temperature evolution in the selective laser sintering process. <https://doi.org/10.1016/j.ijmachtools.2003.10.019> , 2004.
- [46] Y.S. Touloukian, C.Y. Ho, Thermophysical Properties of Matter, IFI/Plenum. New York-Washington.
- [47] Yali Li, Dongdong Gua. Thermal behavior during selective laser melting of commercially pure titanium powder: Numerical simulation and experimental study. <https://doi.org/10.1016/j.addma.2014.09.001> , 2014.

Appendix

```
! /INPUT,HFLUX_func,,,1
*DIM,HEAT_FLX1,TABLE,6,24,1,,,,0 !
!
! Begin of equation: 1.6e9*exp(-2*((X)-.0008256)^2+((Y)-
0.001*(TIME))^2)/2.5e-5^2)
!
*SET,HEAT_FLX1(0,0,1), 0.0, -999
*SET,HEAT_FLX1(2,0,1), 0.0
*SET,HEAT_FLX1(3,0,1), 0.0
*SET,HEAT_FLX1(4,0,1), 0.0
*SET,HEAT_FLX1(5,0,1), 0.0
*SET,HEAT_FLX1(6,0,1), 0.0
*SET,HEAT_FLX1(0,1,1), 1.0, -1, 0, 0, 0, 0, 0
*SET,HEAT_FLX1(0,2,1), 0.0, -2, 0, 1, 0, 0, -1
*SET,HEAT_FLX1(0,3,1), 0, -3, 0, 1, -1, 2, -2
*SET,HEAT_FLX1(0,4,1), 0.0, -1, 0, 2, 0, 0, -3
*SET,HEAT_FLX1(0,5,1), 0.0, -2, 0, 1, -3, 3, -1
*SET,HEAT_FLX1(0,6,1), 0.0, -1, 0, .0008256, 0, 0, 2 % initial position of x
*SET,HEAT_FLX1(0,7,1), 0.0, -3, 0, 1, 2, 2, -1
*SET,HEAT_FLX1(0,8,1), 0.0, -1, 0, 2, 0, 0, -3
*SET,HEAT_FLX1(0,9,1), 0.0, -4, 0, 1, -3, 17, -1
*SET,HEAT_FLX1(0,10,1), 0.0, -1, 0, 0.001, 0, 0, 1 % track velocity
*SET,HEAT_FLX1(0,11,1), 0.0, -3, 0, 1, -1, 3, 1
*SET,HEAT_FLX1(0,12,1), 0.0, -1, 0, 1, 3, 2, -3
*SET,HEAT_FLX1(0,13,1), 0.0, -3, 0, 2, 0, 0, -1
*SET,HEAT_FLX1(0,14,1), 0.0, -5, 0, 1, -1, 17, -3
*SET,HEAT_FLX1(0,15,1), 0.0, -1, 0, 1, -4, 1, -5
*SET,HEAT_FLX1(0,16,1), 0.0, -3, 0, 1, -2, 3, -1
*SET,HEAT_FLX1(0,17,1), 0.0, -1, 0, 2.5e-5, 0, 0, 0 % spot laser radius
*SET,HEAT_FLX1(0,18,1), 0.0, -2, 0, 2, 0, 0, -1
*SET,HEAT_FLX1(0,19,1), 0.0, -4, 0, 1, -1, 17, -2
*SET,HEAT_FLX1(0,20,1), 0.0, -1, 0, 1, -3, 4, -4
*SET,HEAT_FLX1(0,21,1), 0.0, -1, 7, 1, -1, 0, 0
*SET,HEAT_FLX1(0,22,1), 0.0, -2, 0, 1.6e9, 0, 0, -1%
2*absorptivity*power/pi*(radius)^2
*SET,HEAT_FLX1(0,23,1), 0.0, -3, 0, 1, -2, 3, -1
*SET,HEAT_FLX1(0,24,1), 0.0, 99, 0, 1, -3, 0, 0
!
! End of equation: 1.6e9*exp(-2*((X)-.0008256)^2+((Y)-0.001*(TIME))^2)/2.5e-
5^2)
!-->
sf,s1,hflux,%HEAT_FLX1% ! s1 first name selection
```

```
! /INPUT,HFLUX_func,,,1
```

```

*DIM,HEAT_FLX2,TABLE,6,28,1,,,,0 !
! Begin of equation: 1.6e9*exp(-2*((X)+0.0009456)^2+({Y}+0.001*({TIME}-0.5)-
0.0005)^2)/2.5e-5^2)
!
*SET,HEAT_FLX2(0,0,1), 0.0, -999
*SET,HEAT_FLX2(2,0,1), 0.0
*SET,HEAT_FLX2(3,0,1), 0.0
*SET,HEAT_FLX2(4,0,1), 0.0
*SET,HEAT_FLX2(5,0,1), 0.0
*SET,HEAT_FLX2(6,0,1), 0.0
*SET,HEAT_FLX2(0,1,1), 1.0, -1, 0, 0, 0, 0, 0
*SET,HEAT_FLX2(0,2,1), 0.0, -2, 0, 1, 0, 0, -1
*SET,HEAT_FLX2(0,3,1), 0, -3, 0, 1, -1, 2, -2
*SET,HEAT_FLX2(0,4,1), 0.0, -1, 0, 2, 0, 0, -3
*SET,HEAT_FLX2(0,5,1), 0.0, -2, 0, 1, -3, 3, -1
*SET,HEAT_FLX2(0,6,1), 0.0, -1, 0, -0.0009456, 0, 0, 2
*SET,HEAT_FLX2(0,7,1), 0.0, -3, 0, 1, 2, 1, -1
*SET,HEAT_FLX2(0,8,1), 0.0, -1, 0, 2, 0, 0, -3
*SET,HEAT_FLX2(0,9,1), 0.0, -4, 0, 1, -3, 17, -1
*SET,HEAT_FLX2(0,10,1), 0.0, -1, 0, 0.5, 0, 0, 1 % time step to start
next laser
*SET,HEAT_FLX2(0,11,1), 0.0, -3, 0, 1, 1, 2, -1
*SET,HEAT_FLX2(0,12,1), 0.0, -1, 0, 0.001, 0, 0, -3
*SET,HEAT_FLX2(0,13,1), 0.0, -5, 0, 1, -1, 3, -3
*SET,HEAT_FLX2(0,14,1), 0.0, -1, 0, 1, 3, 1, -5
*SET,HEAT_FLX2(0,15,1), 0.0, -3, 0, 0.0005, 0, 0, -1
*SET,HEAT_FLX2(0,16,1), 0.0, -5, 0, 1, -1, 2, -3
*SET,HEAT_FLX2(0,17,1), 0.0, -1, 0, 2, 0, 0, -5
*SET,HEAT_FLX2(0,18,1), 0.0, -3, 0, 1, -5, 17, -1
*SET,HEAT_FLX2(0,19,1), 0.0, -1, 0, 1, -4, 1, -3
*SET,HEAT_FLX2(0,20,1), 0.0, -3, 0, 1, -2, 3, -1
*SET,HEAT_FLX2(0,21,1), 0.0, -1, 0, 2.5e-5, 0, 0, 0
*SET,HEAT_FLX2(0,22,1), 0.0, -2, 0, 2, 0, 0, -1
*SET,HEAT_FLX2(0,23,1), 0.0, -4, 0, 1, -1, 17, -2
*SET,HEAT_FLX2(0,24,1), 0.0, -1, 0, 1, -3, 4, -4
*SET,HEAT_FLX2(0,25,1), 0.0, -1, 7, 1, -1, 0, 0
*SET,HEAT_FLX2(0,26,1), 0.0, -2, 0, 1.6e9, 0, 0, -1
*SET,HEAT_FLX2(0,27,1), 0.0, -3, 0, 1, -2, 3, -1
*SET,HEAT_FLX2(0,28,1), 0.0, 99, 0, 1, -3, 0, 0
!
! End of equation: 1.6e9*exp(-2*((X)+0.0009456)^2+({Y}+0.001*({TIME}-0.5)-
0.0005)^2)/2.5e-5^2)
!-->
sf,s2,hflux,%HEAT_FLX2% ! s1 second name selection
!

```

```

! /INPUT,HFLUX_func,,,1
*DIM,HEAT_FLX3,TABLE,6,28,1,,,,0 !
! Begin of equation: 1.6e9*exp(-2*((X)+0.0010656)^2+({Y}+0.001*({TIME}-1)-
0)^2)/2.5e-5^2)
!
*SET,HEAT_FLX3(0,0,1), 0.0, -999
*SET,HEAT_FLX3(2,0,1), 0.0
*SET,HEAT_FLX3(3,0,1), 0.0
*SET,HEAT_FLX3(4,0,1), 0.0
*SET,HEAT_FLX3(5,0,1), 0.0
*SET,HEAT_FLX3(6,0,1), 0.0
*SET,HEAT_FLX3(0,1,1), 1.0, -1, 0, 0, 0, 0, 0
*SET,HEAT_FLX3(0,2,1), 0.0, -2, 0, 1, 0, 0, -1
*SET,HEAT_FLX3(0,3,1), 0, -3, 0, 1, -1, 2, -2
*SET,HEAT_FLX3(0,4,1), 0.0, -1, 0, 2, 0, 1, -4, 1, -3
*SET,HEAT_FLX3(0,20,1), 0.0, -3, 0, 1, -2, 3, -1
*SET,HEAT_FLX3(0,21,1), 0.0, -1, 0, 2.5e-5, 0, 0, 0

```

```

*SET,HEAT_FLX3(0,22,1), 0.0, -2, 0, 2, 0, 0, -1
*SET,HEAT_FLX3(0,23,1), 0.0, -4, 0, 1, -1, 17, -2
*SET,HEAT_FLX3(0,24,1), 0.0, -1, 0, 1, -3, 4, -4
*SET,HEAT_FLX3(0,25,1), 0.0, -1, 7, 1, -1, 0, 0
*SET,HEAT_FLX3(0,26,1), 0.0, -2, 0, 1.6e9, 0, 0, -1
*SET,HEAT_FLX3(0,27,1), 0.0, -3, 0, 1, -2, 3, -1
*SET,HEAT_FLX3(0,28,1), 0.0, 99, 0, 1, -3, 0, 0
!
! End of equation: 1.6e9*exp(-2*((X)+0.0010656)^2+((Y)+0.001*((TIME)-1)-
0.0005)^2)/2.5e-5^2)
!-->
sf,s3,hflux,%HEAT_FLX3%      ! s3 third name selection
!

```